THE EUROPEAN
PHYSICAL JOURNAL C

Testing symmergent gravity through the shadow image and weak field photon deflection by a rotating black hole using the M87* and Sgr. A* results

Reggie C. Pantig[1,a] , **Ali Övgün**[2,b] , **Durmuş Demir**[3,c]

[1] Physics Department, Mapúa University, 658 Muralla St., Intramuros, 1002 Manila, Philippines
[2] Physics Department, Eastern Mediterranean University, via Mersin 10, 99628 Famagusta, North Cyprus, Turkey
[3] Faculty of Engineering and Natural Sciences, Sabancı University, Tuzla, 34956 Istanbul, Turkey

Abstract In this paper, we study rotating black holes in symmergent gravity, and use deviations from the Kerr black hole to constrain the parameters of the symmergent gravity. Symmergent gravity induces the gravitational constant G and quadratic curvature coefficient c_O from the flat spacetime matter loops. In the limit in which all fields are degenerate in mass, the vacuum energy V_O can be wholly expressed in terms of G and c_O. We parametrize deviation from this degenerate limit by a parameter $\hat{\alpha}$ such that the black hole spacetime is dS for $\hat{\alpha} < 1$ and AdS for $\hat{\alpha} > 1$. In constraining the symmergent parameters c_O and $\hat{\alpha}$, we utilize the EHT observations on the M87* and Sgr. A* black holes. We investigate first the modifications in the photon sphere and shadow size, and find significant deviations in the photonsphere radius and the shadow radius with respect to the Kerr solution. We also find that the geodesics of time-like particles are more sensitive to symmergent gravity effects than the null geodesics. Finally, we analyze the weak field limit of the deflection angle, where we use the Gauss-Bonnet theorem for taking into account the finite distance of the source and the receiver to the lensing object. Remarkably, the distance of the receiver (or source) from the lensing object greatly influences the deflection angle. Moreover, c_O needs be negative for a consistent solution. In our analysis, the rotating black hole acts as a particle accelerator and possesses the sensitivity to probe the symmergent gravity.

1 Introduction

In the Wilsonian sense, quantum field theories (QFTs) are characterized by a classical action and an ultraviolet (UV) cutoff Λ. Quantum loops lead to effective QFTs with loop momenta cut at Λ. The effective QFTs suffer from UV oversensitivity problems: The scalar and gauge boson masses receive $\mathcal{O}(\Lambda^2)$ corrections. The vacuum energy, on the other hand, gets corrected by $\mathcal{O}(\Lambda^4)$ and $\mathcal{O}(\Lambda^2)$ terms. The gauge symmetries get explicitly broken. The question is simple: Can gravity emerge in a way restoring the explicitly broken gauge symmetries? Asking differently, can gravity emerge in a way alleviating the UV oversensitivities of the effective QFT? This question has been answered affirmatively by forming a gauge symmetry-restoring emergent gravity model [1–3]. This model, briefly called as *symmergent gravity*, has been built by the observation that, in parallel with the introduction of Higgs field to restore gauge symmetry for a massive vector boson (with Casimir invariant mass) [4–6], spacetime affine curvature can be introduced to restore gauge symmetries for gauge bosons with loop-induced (Casimir non-invariant) masses proportional to the UV cutoff Λ [1–3]. Symmergent gravity is essentially emergent general relativity (GR) with a quadratic curvature term. It exhibits distinctive signatures, as revealed in recent works on static black hole spacetimes [7–10]. In the present work, we use observational data on M87* and Srg.A* black holes to study symmergent gravity. We focus on rotating black hole spacetimes as these black holes can act as a richer test and analysis laboratory. What we are doing can be viewed as "doing particle physics via black holes" as it will reveal salient properties of the QFT sector through various black hole features.

[a] e-mail: rcpantig@mapua.edu.ph

[b] e-mail: aovgun@gmail.com (corresponding author)
 URL: https://www.aovgun.com

[c] e-mail: durmus.demir@sabanciuniv.edu

In 1919 Arthur Eddington led an expedition to prove Einstein's theory of relativity using gravitational lensing and since then lensing has become an important tool in astrophysics [11–20]. In astrophysics, distances are very important when determining the properties of astrophysical objects. But Virbhadra showed that just the observation of relativistic images without any information about the masses and distances can also accurately give value of the upper bound on the compactness of massive dark objects [21]. Furthermore, Virbhadra proved that there exists a distortion parameter such that the signed sum of all images of singular gravitational lensing of a source identically vanishes (tested with Schwarzschild lensing in weak and strong gravitational fields [22]).

In 2008, Gibbons and Werner used the Gauss-Bonnet theorem (GBT) on the optical geometries in asymptotically flat spacetimes, and calculated weak deflection angle for first time in literature [23]. Afterwards, this method has been applied to various phenomena [24–37]. One of the aims of the present paper is to probe symmergent gravity through the black hole's weak deflection angle using the GBT and also the shadow silhouette as perceived by a static remote observer. In essence, by the very nature of the symmergent gravity, we will be studying the numbers of fermions and bosons and related effects in the vicinity of a spinning black hole, which has the potential to affect the motions of null and time-like geodesics as well as their spin parameter a. (By definition, $a = cJ/GM^2$ where J and M are the angular momentum and mass of the rotation black hole.) Recently, shadow coming from different black hole models has been analyzed extensively in the literature as a probe of the imprints of the astrophysical environment affecting it [38–86] Calculation of the shadow cast of a non-rotating black hole was pioneered by [87,88], and later on extended by [89,90] to an axisymmetric spacetime. Recently, after the detection of gravitational waves in 2015 [91], the first image of the black hole in M87* was formed by the Event Horizon Telescope (EHT) using its electromagnetic spectrum [92]. At the time of writing of this paper, new milestone has been achieved since the EHT revealed the shadow image of the black hole in our galaxy, Sgr. A* [93]. This new result indicates that black hole theory and phenomenology is a hot research topic in view of the rapidly developing observational techniques.

The paper is organized as follows. In Sect. 2, we give a detailed discussion of the symmergent gravity. We give in Sect. 3 the rotating metric, indicating dependence on the symmergent parameters. In Sect. 4, we study the effects of symmergent gravity on null geodesics, which in turn influence the shadow radius and observables associated with it. We also examine the said effect on time-like orbits in the same section. We devote Sect. 5 to investigation of the weak deflection angle at finite-distance, and in Sect. 5.1 we calculate the center-of-mass energy (CM) of two particles and

study particle acceleration near rotating symmergent black hole background. In Sect. 6, we conclude and give future prospects.

2 Symmergent gravity

In this section, we give a brief description of the symmergent gravity in terms of its fundamental parameters. The starting point is quantum field theories (QFTs). Quantum fields are endowed with mass and spin as the Casimir invariant s of the Poincaré group. Fundamentally, QFTs are intrinsic to the flat spacetime simply because they rest on a Poincaré-invariant (translation-invariant) vacuum state [94,95]. Flat spacetime means the total absence of gravity. Incorporation of gravity necessitates the QFTs to be taken to curved spacetime, but this is hampered by Poincaré breaking in curved spacetime [95,96]. This hamper and absence of a quantum theory of gravity [97] together lead one to emergent gravity framework [98–100] as a viable approach.

In general, loss of Poincaré invariance could be interpreted as the emergence of gravity into the QFT [101]. In a QFT, curvature can emerge at the Poincaré breaking sources. One natural Poincaré breakings source is the hard momentum cutoff on the QFT. Indeed, an ultraviolet (UV) cutoff Λ [102] limits momenta p_μ within $-\Lambda^2 \leq \eta^{\mu\nu} p_\mu p_\nu \leq \Lambda^2$ interval as the intrinsic validity edge of the QFT [102]. Under the loop corrections up to the cutoff Λ, the action $S[\eta, \phi, V]$ of a QFT of scalars S and gauge bosons V_μ receives the correction (with $(+, -, -, -)$ metric signature appropriate for QFTs)

$$\delta S[\eta, \phi, V] = \int d^4x \sqrt{-\eta} \left\{ -V_O - c_O \Lambda^4 \right.$$
$$\left. - \sum_i c_{m_i} m_i^2 \Lambda^2 - c_S \Lambda^2 S^\dagger S + c_V \Lambda^2 V_\mu V^\mu \right\} \quad (1)$$

in which $\eta_{\mu\nu}$ is the flat metric, V_O is the vacuum energy which is not power-law in Λ, m_i stands for the mass of a QFT field ψ_i (summing over all the fermions and bosons), and c_O, c_m, c_S and c_V are respectively the loop factors describing the quartic vacuum energy correction, quadratic vacuum energy correction, quadratic scalar mass correction, and the loop-induced gauge boson mass [103,104]. As revealed by the gauge boson mass term $c_V \Lambda^2 V_\mu V^\mu$, the UV cutoff Λ breaks gauge symmetries explicitly since Λ is not a particle mass, that is, Λ is not a Casimir invariant of the Poincaré group. The loop factor c_V (as well as c_S) depends on the details of the QFT. (It has been calculated for the standard model gauge group in [1,2]).

In Sakharov's induced gravity [98,99], the UV cutoff Λ is associated with the Planck scale, albeit with explicitly-broken gauge symmetries and Planckian-size cosmological

constant and scalar masses. In recent years, Sakharov's setup has been approached from a new perspective in which priority is given to the prevention of the explicit gauge symmetry breaking [1]. For this aim, one first takes the effective QFT in (1) to curved spacetime of a metric $g_{\mu\nu}$ such that the gauge boson mass term is mapped as $c_V \Lambda^2 \eta^{\mu\nu} V_\mu V_\nu \longrightarrow c_V V_\mu \left(\Lambda^2 g^{\mu\nu} - R^{\mu\nu}(g) \right) V_\nu$ in agreement with the fact that the Ricci curvature $R^{\mu\nu}(g)$ of the metric $g_{\mu\nu}$ can arise only in the gauge sector via the covariant derivatives [1–3]. One next inspires from the Higgs mechanism to promote the UV cutoff Λ to an appropriate spurion field. Indeed, in parallel with the introduction of Higgs field to restore gauge symmetry for a massive vector boson (Poincare-conserving mass) [4–6], one can introduce spacetime affine curvature to restore gauge symmetries for gauge bosons with loop-induced (Poincare-breaking mass) masses proportional to Λ [1,2,105,106]. Then, one is led to the map

$$\Lambda^2 g^{\mu\nu} \rightarrow \mathbb{R}^{\mu\nu}(\Gamma) \tag{2}$$

in which $\mathbb{R}^{\mu\nu}(\Gamma)$ is the Ricci curvature of the affine connection $\Gamma^\lambda_{\mu\nu}$, which is completely independent of the curved metric $g_{\mu\nu}$ and its Levi-Civita connection [105–107]. This map is analogue of the map $M_V^2 \rightarrow \phi^\dagger \phi$ of the vector boson mass M_V (Poincare conserving) into the Higgs field ϕ. Under the map (2) the effective QFT in (1) takes the form

$$\delta S[g, \phi, V, \mathbb{R}] = \int d^4x \sqrt{-\eta} \left\{ -V_O - \frac{c_O}{16} \mathbb{R}^2(g) \right.$$
$$- \sum_i \frac{c_{m_i}}{4} m_i^2 \mathbb{R}(g) - \frac{c_S}{4} \mathbb{R}(g) S^\dagger S$$
$$\left. + c_V V_\mu \left(\mathbb{R}^{\mu\nu}(\Gamma) - R^{\mu\nu}(g) \right) V_\nu \right\} \tag{3}$$

in which $\mathbb{R}(g) \equiv g^{\mu\nu} \mathbb{R}_{\mu\nu}(\Gamma)$ is the scalar affine curvature [1]. This metric-Palatini theory contains both the metrical curvature $R(g)$ and the affine curvature $\mathbb{R}(\Gamma)$. From the third term, Newton's gravitational constant G is read out to be

$$G^{-1} = 4\pi \sum_i c_{m_i} m_i^2 \xrightarrow{\text{one}} \text{loop} \frac{1}{8\pi} \text{str}\left[\mathcal{M}^2 \right] \tag{4}$$

where $\mathcal{M}^2$ is the mass-squared matrix of all the fields in the QFT spectrum. In the one-loop expression, $\text{str}[\dots]$ stands for super-trace namely $\text{str}[\mathcal{M}^2] = \sum_i (-1)^{2s_i} (2s_i + 1) \text{tr}[\mathcal{M}^2]_{s_i}$ in which $\text{tr}[\dots]$ is the usual trace (including the color degrees of freedom), s_i is the spin of the QFT field ψ_i ($s_i = 0, 1/2, \dots$), and $[\mathcal{M}^2]_{s_i}$ is the mass-squared matrix of the fields having that spin (like mass-squared matrices of scalars ($s_i = 0$), fermions ($s_i = 1/2$) and so on). One keeps in mind that $\text{tr}[\dots]$ encodes degrees of freedom g_i (like color and other degrees of freedom) of the particles.

It is clear that known particles (the standard model spectrum) cannot generate Newton's constant in (4) correctly (in both sign and size). It is necessary to introduce therefore new

particles. Interesting enough, these new particles do not have to couple to the known particles since the only constraint on them is the super-trace in (4) [1,2].

The action (3) remains stationary against variations in the affine connection provided that

$$^\Gamma\nabla_\lambda \mathbb{D}_{\mu\nu} = 0 \tag{5}$$

such that $^\Gamma\nabla_\lambda$ is the covariant derivative of the affine connection $\Gamma^\lambda_{\mu\nu}$, and

$$\mathbb{D}_{\mu\nu} = \left(\frac{1}{16\pi G} + \frac{c_S}{4} S^\dagger S + \frac{c_O}{8} g^{\alpha\beta} \mathbb{R}_{\alpha\beta}(\Gamma) \right) g_{\mu\nu} - c_V V_\mu V_\nu \tag{6}$$

is the field-dependent metric. The motion equation (5) implies that $\mathbb{D}_{\mu\nu}$ is covariantly-constant with respect to $\Gamma^\lambda_{\mu\nu}$, and this constancy leads to the exact solution

$$\Gamma^\lambda_{\mu\nu} = \frac{1}{2} (\mathbb{D}^{-1})^{\lambda\rho} \left(\partial_\mu \mathbb{D}_{\nu\rho} + \partial_\nu \mathbb{D}_{\rho\mu} - \partial_\rho \mathbb{D}_{\mu\nu} \right)$$
$$= {}^g\Gamma^\lambda_{\mu\nu} + \frac{1}{2} (\mathbb{D}^{-1})^{\lambda\rho} \left(\nabla_\mu \mathbb{D}_{\nu\rho} + \nabla_\nu \mathbb{D}_{\rho\mu} - \nabla_\rho \mathbb{D}_{\mu\nu} \right) \tag{7}$$

in which ${}^g\Gamma^\lambda_{\mu\nu}$ is the Levi-Civita connection of the curved metric $g_{\mu\nu}$. The Planck scale in (4) is the largest scale and therefore it is legitimate to make the expansions

$$\Gamma^\lambda_{\mu\nu} = {}^g\Gamma^\lambda_{\mu\nu} + 8\pi G \left(\nabla_\mu \mathbb{D}^\lambda_\nu + \nabla_\nu \mathbb{D}^\lambda_\mu - \nabla^\lambda \mathbb{D}_{\mu\nu} \right) + \mathcal{O}\left(G^2 \right) \tag{8}$$

and

$$\mathbb{R}_{\mu\nu}(\Gamma) = R_{\mu\nu}(g) + 8\pi G \left(\nabla^\alpha \nabla_\mu \mathbb{D}_{\alpha\nu} + \nabla^\alpha \nabla_\nu \mathbb{D}_{\alpha\mu} \right.$$
$$\left. - \Box \mathbb{D}_{\mu\nu} - \nabla_\mu \nabla_\nu \mathbb{D}^\alpha_\alpha \right) + \mathcal{O}\left(G^2 \right) \tag{9}$$

so that both $\Gamma^\lambda_{\mu\nu}$ and $\mathbb{R}_{\mu\nu}(\Gamma)$ contain pure derivative terms at the next-to-leading $\mathcal{O}(G)$ order [2,3]. The expansion in (8) ensures that the affine connection $\Gamma^\lambda_{\mu\nu}$ is solved algebraically order by order in G despite the fact that its motion equation (5) involves its own curvature $\mathbb{R}_{\mu\nu}(\Gamma)$ through $\mathbb{D}_{\mu\nu}$ [105,106]. The expansion (9), on the other hand, ensures that the affine curvature $\mathbb{R}_{\mu\nu}(\Gamma)$ is equal to the metrical curvature $R_{\mu\nu}(g)$ up to a doubly-Planck suppressed remainder. In essence, what happened is that the affine dynamics took the affine curvature $\mathbb{R}$ from its UV value $\Lambda^2_\wp$ in (2) to its IR value R in (9). This way, the GR emerges holographically [108,109] via the affine dynamics such that loop-induced gauge boson masses get erased, and scalar masses get stabilized by the curvature terms. This mechanism renders effective field theories natural regarding their destabilizing UV sensitivities [1,2]. It gives rise to a new framework in which *(i)* the gravity sector is composed of the Einstein-Hilbert term plus a curvature-squared term, and *(ii)* the matter sector is described by an $\overline{MS}$-renormalized QFT [1,2]. We call this framework gauge symmetry-restoring emergent gravity or

simply *symmergent gravity* to distinguish is from other emergent or induced gravity theories in the literature.

It is worth noting that symmergent gravity is not a loop-induced curvature sector in curved spacetime [99,110]. In contrast, symmergent gravity arises when the flat spacetime effective QFT is taken to curved spacetime [1,2] in a way reviving the gauge symmetries broken explicitly by the UV cutoff. All of its couplings are loop-induced parameters deriving from the particle spectrum of the QFT (numbers and masses of particles). It is with these loop features that the GR emerges. In fact, the metric-Palatini action (3) reduces to the metrical gravity theory

$$\int d^4x\sqrt{-g}\left\{-V_{\rm O}-\frac{\mathbb{R}(g)}{16\pi G}-\frac{c_{\rm O}}{16}(\mathbb{R}(g))^2+\frac{c_S}{4}S^\dagger S\,\mathbb{R}(g)\right.$$

$$\left.+c_V{\rm tr}\left[V^\mu\left(\mathbb{R}_{\mu\nu}(\Gamma)-R_{\mu\nu}({}^g\Gamma)\right)V^\nu\right]\right\}$$

$$\xrightarrow{\text{equation (9)}}\int d^4x\sqrt{-g}\left\{-V_{\rm O}-\frac{R}{16\pi G}-\frac{c_{\rm O}}{16}R^2\right.$$

$$\left.-\frac{c_S}{4}S^\dagger S R+\mathcal{O}(G)\right\}\tag{10}$$

after replacing the affine curvature $\mathbb{R}_{\mu\nu}(\Gamma)$ with its solution in (9). Of the parameters of this emergent GR action, Newton's constant G was already defined in (4). The loop factor c_S depends on the underlying QFT. (It reads $c_S\simeq0.29$ in the standard model.) The loop factor $c_{\rm O}$, which was associated with the quartic (Λ^4) corrections in the flat spacetime effective QFT in (1), turned to the coefficient of quadratic-curvature (R^2) term in the symmergent GR action in (10). At one loop, it takes the value

$$c_{\rm O}=\frac{n_{\rm B}-n_{\rm F}}{128\pi^2}\tag{11}$$

in which $n_{\rm B}$ ($n_{\rm F}$) stands for the total number of bosonic (fermionic) degrees of freedom in the underlying QFT (including the color degrees of freedom). Both the $n_{\rm B}$ bosons and $n_{\rm F}$ fermions contain not only the known standard model particles but also the completely new particles. As was commented just above (5), it is a virtue of symmergence that these new particles do not have to couple to the known ones, non-gravitationally.

The last parameter of the symmergent GR action (10) is the vacuum energy density $V_{\rm O}$. It belongs to the non-power-law sector of the flat spacetime effective QFT in (1). At one loop, it takes value (tr[...] involves all degrees of freedom g_i of particles, like color)

$$V_{\rm O}=\frac{{\rm str}\left[\mathcal{M}^4\right]}{64\pi^2}\tag{12}$$

after discarding a possible tree-level contribution. Being a loop-induced quantity, Newton's constant in (4) involves super-trace of (masses)^2 of the QFT fields. In this regard, the potential energy $V_{\rm O}$, involving the super-trace of (masses)^4

of the QFT fields, is expected to expressible in terms of G. To see this, it proves useful to start with mass degeneracy limit in which each and every boson and fermion possess equal masses, $m_b=m_f=M_0$, for all b and f. Needless to say, M_0 is essentially the characteristic scale of the QFT. (Essentially, M_0 is the mean value of all the field masses.) Under this degenerate mass spectrum the potential $V_{\rm O}$ can be expressed as follows:

$$V_{\rm O}=\frac{{\rm str}\left[\mathcal{M}^4\right]}{64\pi^2}=\frac{1}{64\pi^2}\left(\sum_{\rm B}m_{\rm B}^4-\sum_{\rm F}m_{\rm F}^4\right)$$

$$\xrightarrow{\text{mass degeneracy}}\frac{M_0^4}{64\pi^2}(n_{\rm B}-n_{\rm F})=\frac{M_0^2}{8\pi G}=\frac{1}{2(8\pi G)^2c_{\rm O}}\tag{13}$$

where use have been made of the G formula in (4) and $c_{\rm O}$ formula in (11). Now, the problem is to take into account realistic cases in which the QFT fields are not all mass-degenerate. For a QFT with characteristic scale M_0 but with no detailed knowledge of the mass spectrum, realistic cases might be represented by parametrizing the potential energy as

$$V_{\rm O}=\frac{1-\hat{\alpha}}{(8\pi G)^2c_{\rm O}}\tag{14}$$

in which the new parameter $\hat{\alpha}$ is introduced as a measure of the deviations of the boson and fermion masses from the QFT characteristic scale M_0. Clearly, $\hat{\alpha}=1/2$ corresponds to the degenerate case in (13). Alternatively, $\hat{\alpha}=1$ represents the case in which $\sum_{\rm B}m_{\rm B}^4=\sum_{\rm F}m_{\rm F}^4$ in (13). In general, $\hat{\alpha}>1$ ($\hat{\alpha}<1$) corresponds to the boson (fermion) dominance in terms of the trace (masses)^4.

Symmergence makes gravity emerge from within the flat spacetime effective QFT. Fundamentally, as follows from the action (1), Newton's constant G in (4), the quadratic curvature coefficient $c_{\rm O}$ in (11), and the vacuum energy $V_{\rm O}$ in (12) transpired in the flat spacetime effective QFT from the matter loops. (The loop factor c_S and similar parameters couple the matter fields.) Once the gravity emerges as in (10), however, G, $c_{\rm O}$ and $V_{\rm O}$ gain a completely new physical meaning as the curvature sector parameters (not involving the matter fields). In this sense, they are symmergent gravity parameters in the sense that they became curvature sector parameters via the symmergence.

A glance at the second line of (10) reveals that symmergent gravity is an $R+R^2$ gravity theory with non-zero cosmological constant. In fact, it can be put in the form

$$S=\frac{1}{16\pi G}\int d^4x\sqrt{-g}\left(R+f(R)\right)\tag{15}$$

after leaving aside the scalars S and the other matter fields, after switching to $(-,+,+,+)$ metric signature (appropriate for the black hole analysis in the sequel), and after introduc-

ing the $f(R)$ gravity function

$$f(R) = -\pi G c_O R^2 - 16\pi G V_O \qquad (16)$$

comprising the vacuum energy V_O and the quadratic-curvature term proportional to c_O. The Einstein field equations arising from the action (15)

$$R_{\mu\nu}(1 + f'(R)) - \frac{1}{2} g_{\mu\nu}(R + f(R))$$
$$+ (\nabla_\mu \nabla_\nu - \Box g_{\mu\nu}) f'(R) = 0 \qquad (17)$$

become $R_0(f'(R_0) - 1) - 2f(R_0) = 0$ upon contraction at constant curvature ($R = R_0$), and possess the solution [111,112]

$$R_0 = 32\pi G V_O = \frac{1 - \hat{\alpha}}{2\pi G c_O} \qquad (18)$$

after using the vacuum energy formula in (14) in the second equality. It is clear that this R_0 value would vanish if the vacuum energy were not nonzero. Indeed, for a quadratic gravity with $f(R) = bR^2$ one gets the solution $R_0 = 0$. But for a quadratic gravity like $f(R) = a + bR^2$ one finds $R_0 = -2a \neq 0$, which reduces to the R_0 in (18) for $a = -16\pi G V_O$.

The Einstein field equations (17) possess static, spherically-symmetric, constant-curvature solutions of the form [111, 112]

$$ds^2 = -h(r)dt^2 + \frac{dr^2}{h(r)} + r^2(d\theta^2 + \sin^2\theta d\phi^2) \qquad (19)$$

in which

$$h(r) = 1 - \frac{2GM}{r} - \frac{(1 - \hat{\alpha})}{24\pi G c_O} r^2 \qquad (20)$$

is the lapse function following from (18). In the sequel, we will analyze this constant-curvature configuration ($R = R_0 \neq 0$) in both the dS ($V_O > 0$ namely $\hat{\alpha} < 1$) and AdS ($V_O < 0$ namely $\hat{\alpha} > 1$) spacetimes in the case of rotating black holes. We will use rotating black hole properties to determine or constrain the model parameters c_O and $\hat{\alpha}$.

3 Rotating black holes in symmergent gravity

Appropriate for a rotating black hole geometry, we use Boyer–Lindquist coordinates with a metric free of the coordinate singularities in the spacetime both exterior to the black hole and interior to the cosmological horizon. The metric is given by [111,113–117]

$$ds^2 = \frac{\rho^2}{\Delta_r} dr^2 + \frac{\rho^2}{\Delta_\theta} d\theta^2 + \frac{\Delta_\theta \sin^2\theta}{\rho^2} \left[a dt - (r^2 + a^2) \frac{d\phi}{\Xi} \right]^2$$
$$- \frac{\Delta_r}{\rho^2} \left(dt - a \sin^2\theta \frac{d\phi}{\Xi} \right)^2 \qquad (21)$$

with the various quantities

$$\Delta_r = (r^2 + a^2) \left(1 - \frac{r^2}{3} \frac{(1 - \hat{\alpha})}{8\pi c_O} \right) - 2Mr, \qquad (22)$$

$$\rho^2 = r^2 + a^2 \cos^2\theta, \qquad (23)$$

$$\Delta_\theta = 1 + \frac{r^2}{3} \frac{(1 - \hat{\alpha})}{8\pi c_O} a^2 \cos^2\theta, \qquad (24)$$

$$\Xi = 1 + \frac{r^2}{3} \frac{(1 - \hat{\alpha})}{8\pi c_O} a^2. \qquad (25)$$

Here, a is the black hole spin parameter, and $\hat{\alpha}$ and c_O are the parameters of the symmergent gravity. The physical energy E and angular momentum J of the black hole are related to the parameters M and a via the relations [118,119]

$$E = \frac{M}{\Xi^2}, \quad J = \frac{aM}{\Xi^2} \qquad (26)$$

in which M is the root of the equation $\Delta_r(r_+) = 0$ namely

$$M = \frac{1}{2r_+} (r_+^2 + a^2) \left(1 - \frac{r_+^2}{3} \frac{(1 - \hat{\alpha})}{8\pi c_O} \right) \qquad (27)$$

where r_+ is the radius of the event horizon. In this way, one can express energy and angular momentum in terms of the parameters r_+, a, and G. (One here notes that $\frac{1}{l^2} = \frac{(\hat{a}-1)}{24\pi G c_O}$, where the curvature radius l is related to the negative cosmological constant as $\Lambda = -3 l^{-2}$). As a result, one finds

$$E = \frac{1}{2\Xi^2 r_+} \left(r_+^2 + a^2 + \frac{r_+^4}{l^2} + \frac{a^2 r_+^2}{l^2} \right),$$
$$J = \frac{a}{2\Xi^2 r_+} \left(r_+^2 + a^2 + \frac{r_+^4}{l^2} + \frac{a^2 r_+^2}{l^2} \right) \qquad (28)$$

as the explicit expressions for the definitions in (26).

Numerically, horizons can be determined by analyzing the lapse function, that is, by solving $\Delta_r = 0$ using its definition in (22). Besides, the location of the ergoregions can be determined numerically by plotting the metric component g_{tt} and looking for points satisfying $g_{tt} = 0$. In fact, plotted in Fig. 1 are Δ_r and g_{tt} as functions of r for the integration constant $\hat{\alpha}$ of 0.90 and 1.10, black hole spin parameter $a = 0.9 M$, and the various values of c_O. In general, symmergent black hole can mimic the dS ($\hat{\alpha} > 1$) or AdS-Kerr ($\hat{\alpha} < 1$) black holes depending on the sign of $\hat{\alpha}$. But, as already shown by Pogosian and Silvestri [120], consistent f(R) gravity theories require $\frac{dF(R)}{dR} > 0$ in order to remain stable the (non-tachyonic scalaron). This constraint imposes the condition $c_O < 0$ on the loop-induced quadratic curvature coefficient, and restricts viable solutions to the AdS-Kerr type. In view of the underlying QFT, $c_O < 0$ implies that $n_F > n_B$ – a mostly fermionic QFT [1–3]. In the extreme case of no new bosons (in agreement with $n_F > n_B$), one finds out that the new particle sector remains inherently stable thanks to the fact that

fermion masses do not have any power-law sensitivity to the UV cutoff.

Usually, value of the cosmological constant is scaled to a higher value to see its overall effect. In this sense, assumed values of $\hat{\alpha}$ and c_O are also rescaled similarly. As is seen from Fig. 1, null boundaries are greatly affected by the values of the symmergent parameters $\hat{\alpha}$ and c_O. Indeed, $\hat{\alpha} > 1$ leads to three horizons where, in the context of the dS geometry, the third horizon corresponds to the cosmic outer boundary. It shifts farther as c_O gets more negative. The two remaining null boundaries are the Cauchy and event horizons. In constrast to the dS solution, the symmergent AdS solution gives only two horizons such that symmergent effects are nearly vanishingly small on the inner horizon compared to the outer horizon. As for the ergoregions, $\hat{\alpha} > 1$ leads to three ergoregions, and it can be seen that the farthest one turns out to be even beyond the cosmic horizon.

The Hawking temperature is given by

$$T = \frac{\kappa}{2\pi} \tag{29}$$

such that the surface gravity

$$\kappa^2 = -\frac{1}{2} \nabla^\mu \chi^\nu \nabla_\mu \chi_\nu \tag{30}$$

involves the null Killing vectors χ^ν. The two Killing vectors $\xi^\nu = \partial_t$ and $\zeta^\nu = \partial_\varphi$ in the metric are associated with the time translation and rotational invariance, respectively. Consequently, we take

$$\chi^\nu = \xi^\nu + \Omega \zeta^\nu \tag{31}$$

and determine Ω under the condition that χ^ν is a null vector. This leads to the constraint

$$\chi^\nu \chi_\nu = g_{tt} + 2\Omega g_{t\varphi} + \Omega^2 g_{\varphi\varphi} = 0, \tag{32}$$

from which one gets

$$\Omega = -\frac{g_{t\varphi}}{g_{\varphi\varphi}} \pm \sqrt{\left(\frac{g_{t\varphi}}{g_{\varphi\varphi}}\right)^2 - \frac{g_{tt}}{g_{\varphi\varphi}}} \tag{33}$$

which reduces to

$$\Omega_+ = \frac{a\,\Xi}{r_+^2 + a^2} \tag{34}$$

at the event horizon $\Delta(r_+) = 0$. For this Ω value one then gets

$$\kappa = \frac{1}{2\left(r_+^2 + a^2\right)} \frac{d\Delta_r}{dr}\bigg|_{r=r_+}, \tag{35}$$

for the surface gravity,

$$T = \frac{r_+}{4\pi\left(r_+^2 + a^2\right)} \left(1 + \frac{a^2}{l^2} + \frac{3r_+^2}{l^2} - \frac{a^2}{r_+^2}\right)$$

$$= \frac{3r_+^4 + \left(a^2 + l^2\right)r_+^2 - l^2 a^2}{4\pi l^2 r_+ \left(r_+^2 + a^2\right)} \tag{36}$$

for the Hawking temperature, and

$$S = \frac{A}{4} = \frac{\pi\left(r_+^2 + a^2\right)}{\Xi} \tag{37}$$

for the Bekenstein-Hawking entropy. Needless to say, all thermodynamic quantities are necessarily non-negative. The rotating symmergent black hole satisfies therefore the first law of thermodynamics

$$dE = TdS + \Omega dJ \tag{38}$$

with

$$\Omega = \frac{a\left(1 + r_+^2 l^{-2}\right)}{r_+^2 + a^2}. \tag{39}$$

4 Geodesics around rotating symmergent black holes

In this section we give a detailed analysis of the geodesics and orbits around the symmergent black holes.

4.1 Null geodesic and shadow cast

We start the analysis with null geodesics. The Hamilton–Jacobi equation gives

$$\frac{\partial S}{\partial \lambda} = -H, \tag{40}$$

where S is the Jacobi action in terms of the affine parameter λ (proper time) and coordinates x^μ. The Hamiltonian is given by

$$H = \frac{1}{2} g^{\mu\nu} \frac{\partial S}{\partial x^\mu} \frac{\partial S}{\partial x^\nu}, \tag{41}$$

in the GR so that

$$\frac{\partial S}{\partial \lambda} = -\frac{1}{2} g^{\mu\nu} \frac{\partial S}{\partial x^\mu} \frac{\partial S}{\partial x^\nu} \tag{42}$$

as follows from (40) above. Using the separability ansatz for the Jacobi function

$$S = \frac{1}{2} \mu^2 \lambda - Et + L\phi + S_r(r) + S_\theta(\theta), \tag{43}$$

with the particle mass μ, one is led to the following first-order motion equations [121]

$$\Sigma \frac{dt}{d\lambda} = \frac{\Xi(r^2 + a^2)P(r)}{\Delta_r} - \frac{\Xi a P(\theta)}{\Delta_\theta},$$

$$\Sigma \frac{dr}{d\lambda} = \sqrt{R(r)},$$

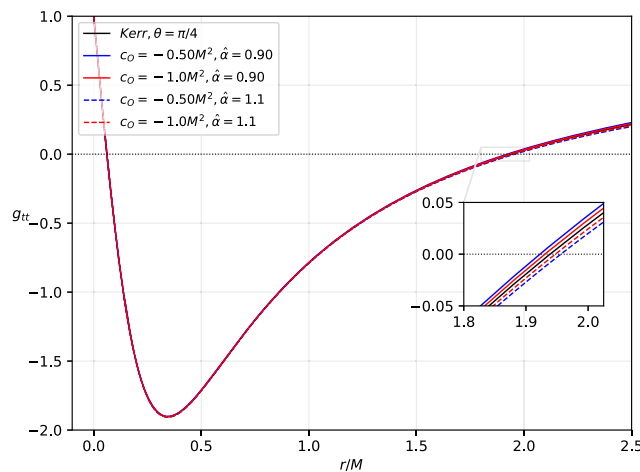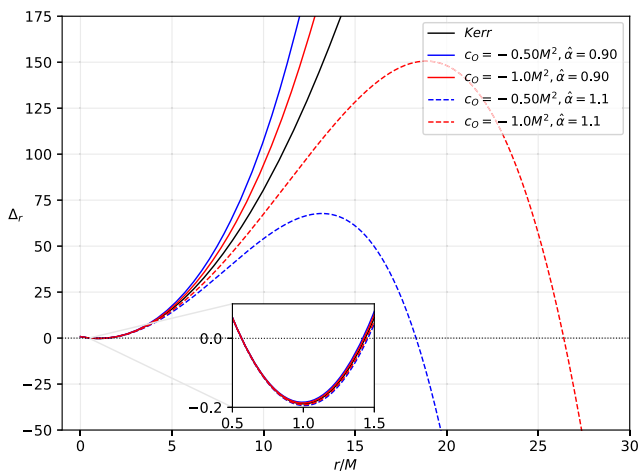$$\Sigma \frac{d\theta}{d\lambda} = \sqrt{\Theta(\theta)},$$

Fig. 1 Variations of the functions Δ_r (left panel) and g_{tt} (right panel) with the radial coordinate r for the black hole spin parameter $a = 0.9\,M$. The plots show the null boundaries, with solid (dashed) lines mimicking the behavior of AdS (dS) black holes. We consider only negative values of c_O in agreement with [120]

$$\Sigma \frac{d\phi}{d\lambda} = \frac{\Xi a P(r)}{\Delta_r} - \frac{\Xi P(\theta)}{\Delta_\theta \sin^2 \theta} \qquad (44)$$

after introducing the functions

$$
\begin{aligned}
R(r) &= P(r)^2 - \Delta_r(\mu^2 r^2 + K), \\
P(r) &= \Xi E(r^2 + a^2) - \Xi a L, \\
\Theta(\theta) &= \Delta_\theta(K - \mu^2 a^2 \cos^2 \theta) - \frac{P(\theta)^2}{\sin^2 \theta}, \\
P(\theta) &= \Xi(a E \sin^2 \theta - L).
\end{aligned}
\qquad (45)
$$

From the third equation in (44) above, constants of motion can be correlated via the relation $K = \Xi^2(aE - L)^2$, which is a consequence of a hidden symmetry in the θ-coordinate [121,122].

First, we study null geodesic and shadow cast for massless particles ($\mu = 0$). Photon circular orbits, which are always unstable, must then satisfy the following condition

$$R(r) = \frac{dR(r)}{dr}\Big|_{r=r_o} = 0. \qquad (46)$$

The null geodesic is important is an important quantity for symmergent black holes. We need, in particular, the photon region in constant r_0, the so-called photonsphere, which is an unstable orbit. The shadow cast ultimately depends on the photon region. With $\mu = 0$, it proves convenient to define these two impact parameters

$$\xi = \frac{L}{E} \quad \text{and} \quad \eta = \frac{K}{E^2}. \qquad (47)$$

These parameters are found to possess the following explicit expressions

$$\xi = \frac{\Delta_r'(r^2 + a^2) - 4\Delta_r r}{a \Delta_r'}, \qquad (48)$$

$$\eta = \frac{-r^4 \Delta_r'^2 + 8r^3 \Delta_r \Delta_r' + 16r^2 \Delta_r(a^2 - \Delta_r)}{a^2 \Delta_r'^2} \qquad (49)$$

after a lengthy algebra. The photonsphere radius r_{ph} can then be determined by solving $\eta(r) = 0$ for r. The analytical solutions are well-known for both Schwarzschild and Kerr black holes. In our case, we plot (49) in Fig. 2 to get the qualitative impression about the location of r_{ph}. The left panel of Fig. 2 concerns location of the photonsphere along the equatorial plane. As we would expect, the Schwarzschild case gives $r_{\mathrm{ph}} = 3M$. The extreme Kerr case gives two possible locations, that is, the prograde orbit at $r_{\mathrm{ph}} = M$ and the retrograde orbit at $r_{\mathrm{ph}} = 4M$. The plot shows the locations for $a = 0.90M$, which fall near the said extreme values. For the symmergent effect, the dS type (dashed lines) gives slightly lower values in the retrograde case while the AdS type gives a larger one. It is clear that the more negative the c_O the closer the photon ring to the Kerr case. The symmergent effect is also present in the prograde case though the deviation is smaller than in the retrograde case. In the right panel of Fig. 2, we consider photons with zero angular momentum, that is, those that traverse the equatorial plane in a perpendicular manner (the so-called nodes). The retrograde case gives higher values for such an orbit than the prograde case. The deviation caused is barely evident, especially in the prograde case (the inset highlights the deviation). As a final remark, we note that the symmergent effect mimics dS or AdS cases, where such a behavior does not occur in the Schwarzschild case. The coupling between the spin and sym-

mergent parameters made it possible to affecy the behavior of the photonsphere.

Escaping photons in the unstable orbit gives the possibility for remote observers to backward-trace and obtain a shadow cast by using the celestial coordinates (r_{obs}, θ_{obs}). Such an observer is also known as the Zero Angular Momentum Observer (ZAMO). Also, in this type of co-moving frame, without loss of generality, one makes the approximation $r_{obs} \to \infty$ and takes $\theta_{obs} = \pi/2$. The celestial coordinates are defined as [123]

$$
\begin{aligned}
\mathcal{X} &= -r_{obs} \frac{\xi}{\zeta \sqrt{g_{\phi\phi}} \left(1 + \frac{g_{t\phi}}{g_{\phi\phi}}\xi\right)}, \\
\mathcal{Y} &= r_{obs} \frac{\pm\sqrt{\Theta(i)}}{\zeta \sqrt{g_{\theta\theta}} \left(1 + \frac{g_{t\phi}}{g_{\phi\phi}}\xi\right)},
\end{aligned}
\tag{50}
$$

and the condition $r_{obs} \to \infty$ leads to the simplified relations

$$
\begin{aligned}
\mathcal{X} &= -\xi \csc\theta_{obs}, \\
\mathcal{Y} &= \pm\sqrt{\eta + a^2 \cos^2\theta_{obs} - \xi^2 \cot^2\theta_{obs}}.
\end{aligned}
\tag{51}
$$

These expressions further simplify to $\mathcal{X} = 0$ and $\mathcal{Y} = \pm\sqrt{\eta}$ when $\theta_{obs} = \pi/2$. If, furthermore, $a = 0$ then shadow cast of a Schwarzschild black hole (a circle) is obtained. The plot of $\mathcal{Y}$ vs. $\mathcal{X}$ is shown in Fig. 3 for the black hole spin parameter value of $a = 0.90M$.

Overall, we observe the D-shaped nature of the shadow cast due to the spin parameter. Considering first the effect of the inclination angle, we see that as we decrease the value of θ (going up from the equatorial plane), we see that the shape changes. Remarkably, in the upper right figure, the shape becomes more compressed in the α axis, and as one continues to go up (lower left figure), it goes back to an almost spherical shape. Finally, near the pole, a drastic change in the shadow shape occurs due to stretching of the α-axis. For the symmergent effects, we note that the dS type tends to decrease the photonsphere radius. Nevertheless, as photons travel in the intervening space under the effect of the symmergent parameter the shadow size is seen to increase. We can see the contrast in the AdS type symmergent effect in that while the photonsphere increases the shadow size tends to decrease.

In the azimuthal plane, we see how the shadow becomes "D-shaped" when the balck hole spin parameter a is near extremal. The numerical value of the shadow radius associated with this shape [59] can be calculated [40] by using

$$
R_s = \frac{\mathcal{Y}_t^2 + (\mathcal{X}_t - \mathcal{X}_r)^2}{2|\mathcal{X}_t - \mathcal{X}_r|}
\tag{52}
$$

which we plot in Fig. 4 (upper left), along with the shadow's angular radius θ_{sh} (upper right), where the latter is defined by

$$
\theta_{sh} = 9.87098 \times 10^{-3} \frac{R_s M}{D}
\tag{53}
$$

after taking the black hole mass M in units of $M_\odot$ and D in parsecs. We emphasize that these behaviors are consistent with Fig. 3. Other observables that can be derived from the shadow are the distortion parameter δ_s and the energy emission rate $\frac{d^2E}{d\omega dt}$, which are defined as

$$
\delta_s = \frac{d_s}{R_s} = \frac{\tilde{\mathcal{X}}_l - \mathcal{X}_l}{R_s},
\tag{54}
$$

$$
\frac{d^2E}{d\omega dt} = 2\pi^2 \frac{\Pi_{ilm}}{e^{\omega/T} - 1}\omega^3
\tag{55}
$$

such that the energy absorption cross-section can be approximated as $\Pi_{ilm} \sim \pi R_s^2$ for an observer at $r_{obs} \to \infty$. These observables are plotted in Fig. 4 in the lower two panels. From these panels we are able to see how the spin parameter increases the distortion of the shadow. We can also see that even if the dS symmergent effect tends to increase the shadow, the distortion it gives is smaller than the AdS symmergent effect. In the lower right panel of Fig. 4, we comparatively show $a = 0.25M$ and $a = 0.90M$ for the Kerr, dS and AdS symmergent black holes. For the Kerr case, we see that low values of a leads to higher values for energy emission rate and peak frequency. Adding the symmergent effect at low values of a and $\hat{\alpha} = 0.90$, we see that a less negative c_O provides the highest peak frequency and energy emission rate. For $\hat{\alpha} = 1.1$, this very same c_O gives the lowest emission rate and peak frequency. For $a = 0.90M$, we observe in the inset plot that the roles are reversed near the peak of the curve. We see that there is a point in the plot where the behavior flips as the frequency σ increases whilst the emission rate decreases.

We now investigate observational constraints on the symmergent parameter c_O using the black hole shadow data collected from M87* [124] and Sgr. A* [93]. The data is tabulated in Table 1. With these data, one can determine diameter of the shadow size in units of the black hole mass with

$$
d_{sh} = \frac{D\theta}{M}.
\tag{56}
$$

In this sense, the diameter of the shadow image of M87* and Sgr. A* are $d_{sh}^{M87*} = (11 \pm 1.5)m$ and $d_{sh}^{Sgr.\ A*} = (9.5 \pm 1.4)m$, respectively. Meanwhile, the theoretical shadow diameter can be obtained via $d_{sh}^{theo} = 2R_{sh}$ with the use of Eq. (52). Based on Fig. 5, we can conclude that the parameters we used in describing the shadow cast fall within the upper and lower bounds at the 1σ level. Where this happens, the range in c_O is more extensive in M87* than in Sgr. A*. We also observe that less negative c_O introduces more sensitivity to deviation than more negative c_O (Table 2).
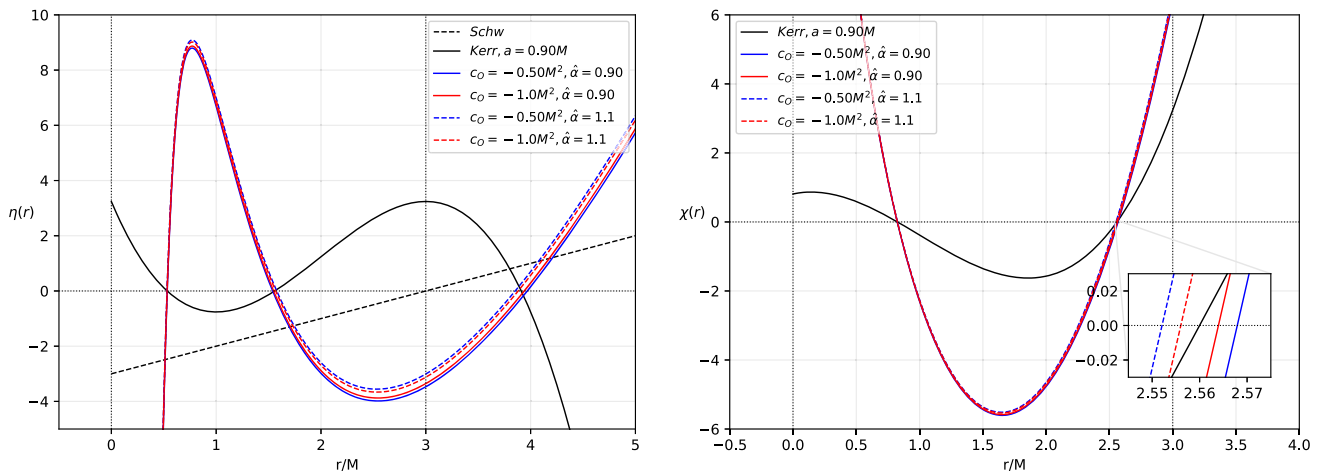
Fig. 2 Location of the photonsphere (left panel), and location of the photonsphere crossing at $\phi = 0$ or along the equatorial plane (right panel). We take $a = 0.90M$ in both plots (a is the black hole spin parameter)
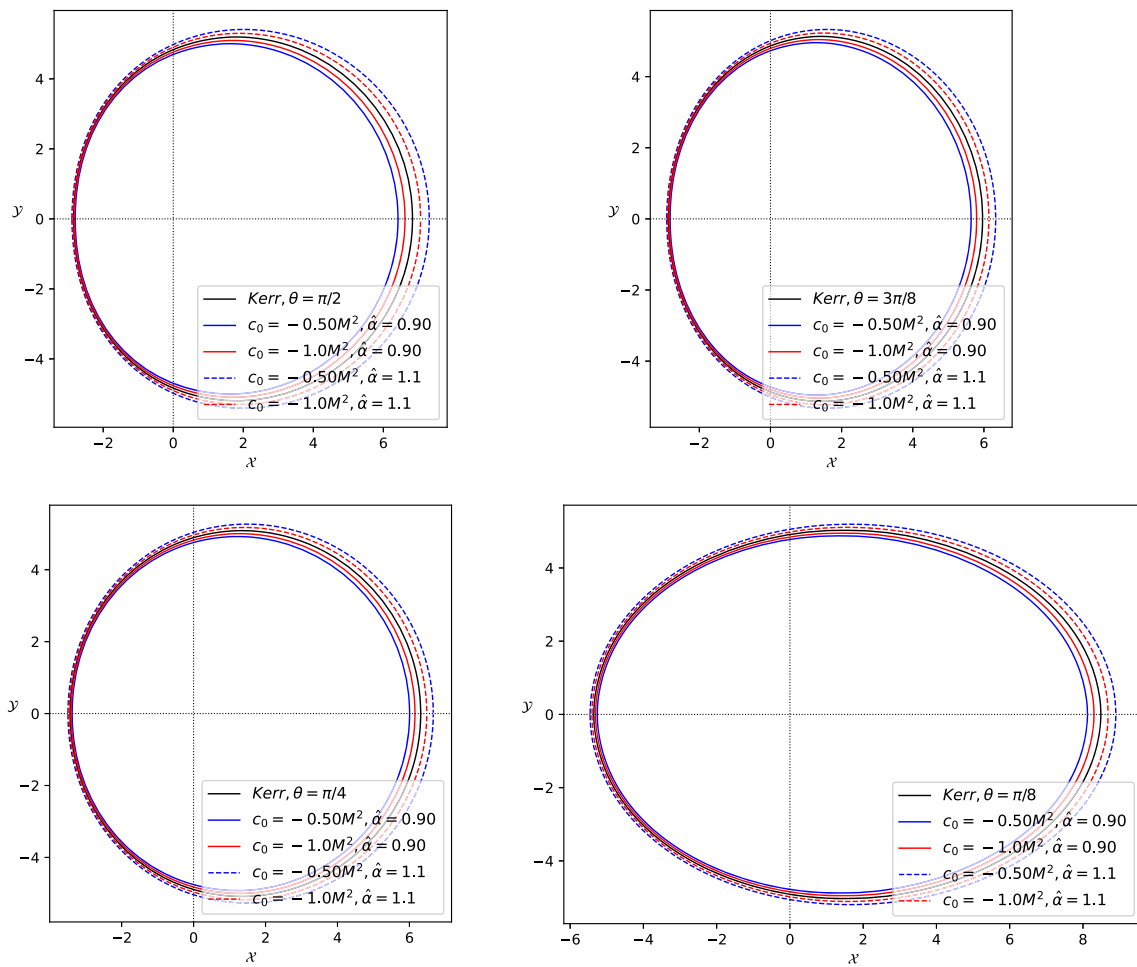

Fig. 3 Shadow plot for different inclination angles for the black hole spin parameter $a = 0.90M$ (aspect ratios of figures are set to obtain the actual view)
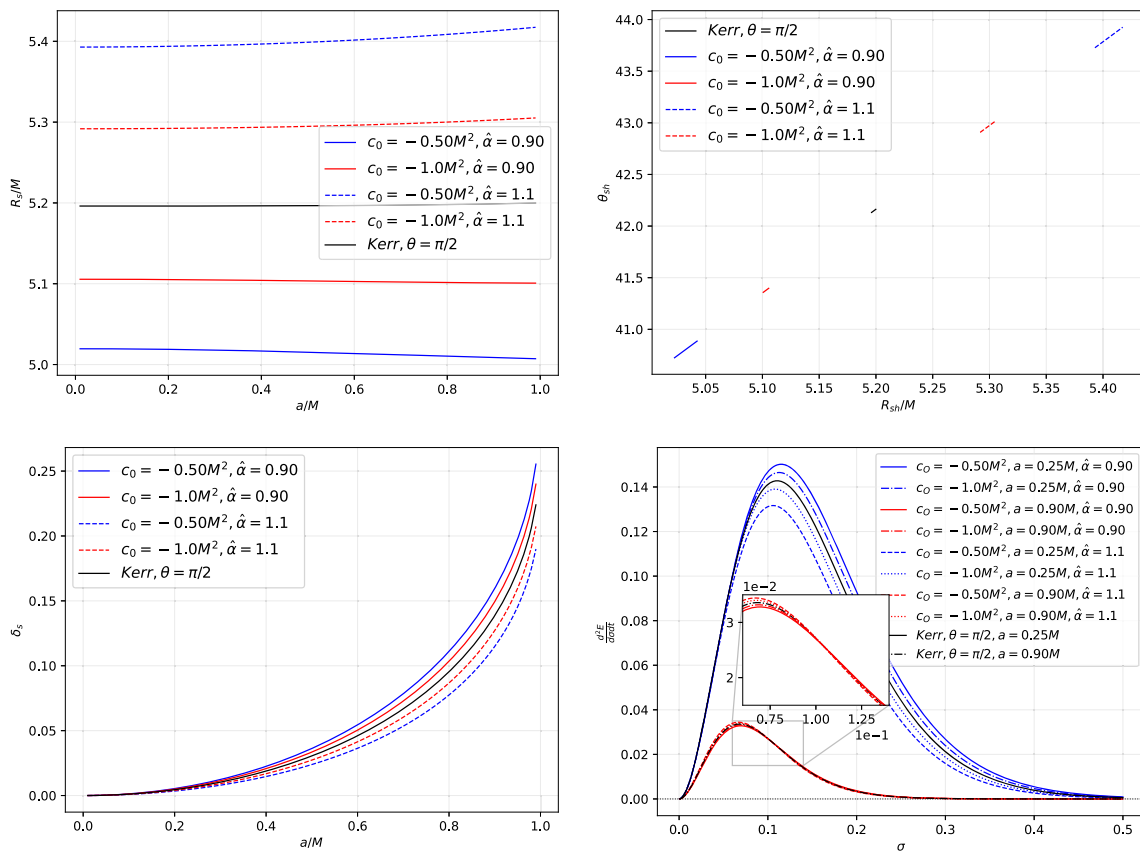
Fig. 4 Shadow observables associated with the upper left panel of Fig. 3. Shown here are shadow radius (upper-left panel), angular diameter in μas for M87* (upper-right panel), distortion parameter (lower-left panel), and energy emission rate (lower-right panel)

Table 1 Black hole observational constraints

Black hole	Mass ($M_\odot$)	Angular diameter: $2\theta_{sh}$ (μas)	Distance (kpc)
Sgr. A*	$4.3 \pm 0.013 \times 10^6$ (VLTI)	48.7 ± 7 (EHT)	8.277 ± 0.033
M87*	$6.5 \pm 0.90 \times 10^9$	42 ± 3	16800
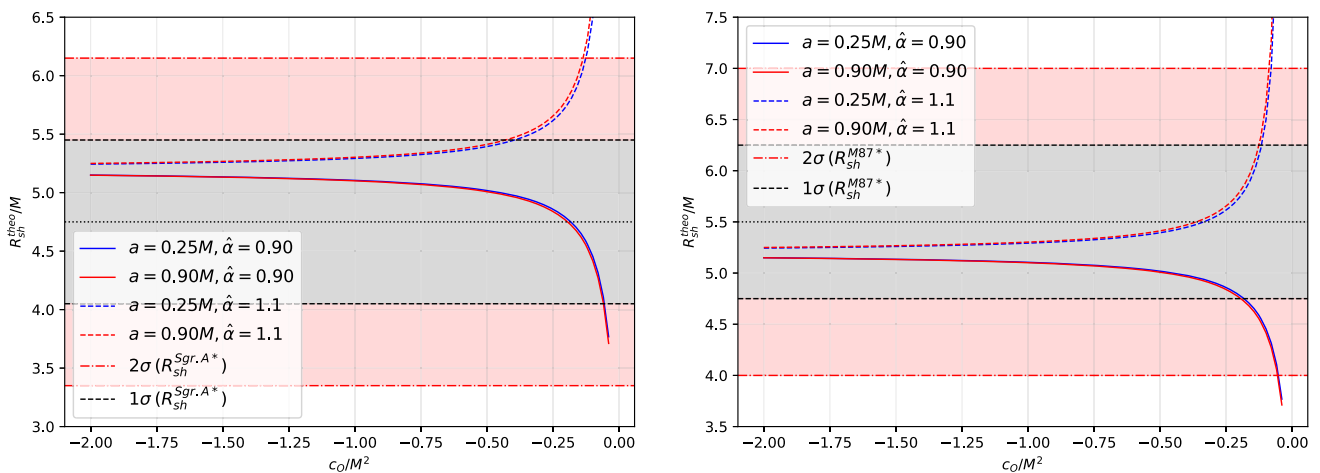
Fig. 5 Constraint on the symmergent gravity parameter c_O by the Sgr. A* data (left-panel) and M87* data (right-panel)

Table 2 Bounds on c_0 as read off from the curves in Fig. 5

	2σ		1σ		Observed R_{sh}
Sgr. A*					
Spin a ($\hat{\alpha} = 0.90$)	Upper	Lower	Upper	Lower	Mean
0.25M	–	–	–	− 0.057	− 0.184
0.90M	–	–	–	− 0.060	− 0.196
Spin a ($\hat{\alpha} = 1.10$)	Upper	Lower	Upper	Lower	Mean
0.25M	− 0.127	–	− 0.397	–	–
0.90M	− 0.137	–	− 0.431	–	–
M87*					
Spin a ($\hat{\alpha} = 0.90$)	Upper	Lower	Upper	Lower	Mean
0.25M	–	− 0.054	–	− 0.196	–
0.90M	–	− 0.057	–	− 0.185	–
Spin a ($\hat{\alpha} = 1.10$)	Upper	Lower	Upper	Lower	Mean
0.25M	− 0.081	–	− 0.117	–	− 0.336
0.90M	− 0.089	–	− 0.128	–	− 0.364

4.2 Symmergent gravity effects on time-like orbits: effective potential and ISCO radii

We now turn our attention to time-like orbits. Here, we will still use the equations of motion from the Hamilton–Jacobi approach but this time set $\mu = 1$. We are interested in determining the radius of the innermost stable circular orbit (ISCO), which is very important in the study of matter accretion disks and in the study also of the effective potential for getting a qualitative description of bound and unbound orbits under the symmergent effects.

To determine the qualitative behavior of massive particle's motion around the symmergent black hole (i.e. bound, stable and unstable circular orbits), we use the effective potential formula [125]

$$V_{\pm} = \frac{g^{t\phi}}{g^{tt}} L \pm \left\{ \left[\left(\frac{g^{t\phi}}{g^{tt}} \right)^2 - \frac{g^{\phi\phi}}{g^{tt}} \right] L^2 - \frac{1}{g^{tt}} \right\}^{1/2}. \quad (57)$$

written in terms of the inverse metric $g^{\mu\nu}$ and angular momentum L. Shown in Fig. 6 is the effective potential for $L = \pm 3.50M$. In this figure, maxima and minima correspond to the unstable and stable circular orbits, respectively. One notes that for $a = 0$ (Schwarzschild) case, the maxima of the effective potential curve are way lower compared to when $a = 0.90M$ (Kerr case). We can see that the energy for an unstable circular orbit is higher in the AdS symmergent effect, where less negative c_0 giving the highest energy. Its minima, which represents the stable circular orbit, has a greater radius for more negative c_0. Peculiar as it may seem, particles with energies higher that than the peak energy tend to get deflected back when it reaches at some radial point near the cosmic horizon (one recalls that we scaled the Symmergent dS and AdS parameters). As for the dS symmergent

effect, we can see that the least negative c_O gives the lowest peak energy in the unstable circular orbit. Particles with low energy are deflected back to $r \to \infty$ when they reach low values of r. While the AdS type can have elliptical bound orbits the same way as in the Kerr case, we see that dS type does not admit such orbit as far as the value of the angular momentum used herein is concerned. In Fig. 6 (right-panel), we plotted also the effective potential in which the particle attains a negative angular momentum. It is known that it does not happen in the Schwarzschild case. As we can see in the right-panel, particles with negative energies can be created near the rotating black hole's event horizon. Clearly, symmergent gravity affects the particle's energy, which in turn contributes to the Penrose process and black hole evaporation.

The ISCO radius occurs when the maximum and minimum of the effective potential curve merge in an inflection point for a given value of L. It is clear that we have two separate cases for ISCO determination since we need to consider both the prograde and retrograde motion of the time-like particles. Besides, such a circular orbit is only marginally stable, which means that any inward perturbation will lead the particle to spiral toward the event horizon. In locating the ISCO radius, we use Eq. (46) and solve for the energy E_{cir}. One starts with [121,126],

$$X^2 = L - aE = \frac{r^3 \left(\Delta_r' - 2E_{\text{cir}}^2 r \right)}{-2a^2 - r\Delta_r' + 2\Delta_r}. \quad (58)$$

Differentiating equation (58) with respect to r and after some algebra we get ($E_{\text{cir}} = E_{\text{isco}}$)

$$E_{\text{isco}}^2 = \frac{1}{Br} \left\{ a^2 \left[- \left(r\Delta_r'' + 3\Delta_r' \right) \right] + r\Delta_r \Delta_r'' - 2r\Delta_r'^2 + 3\Delta_r \Delta_r' \right\}, \quad (59)$$
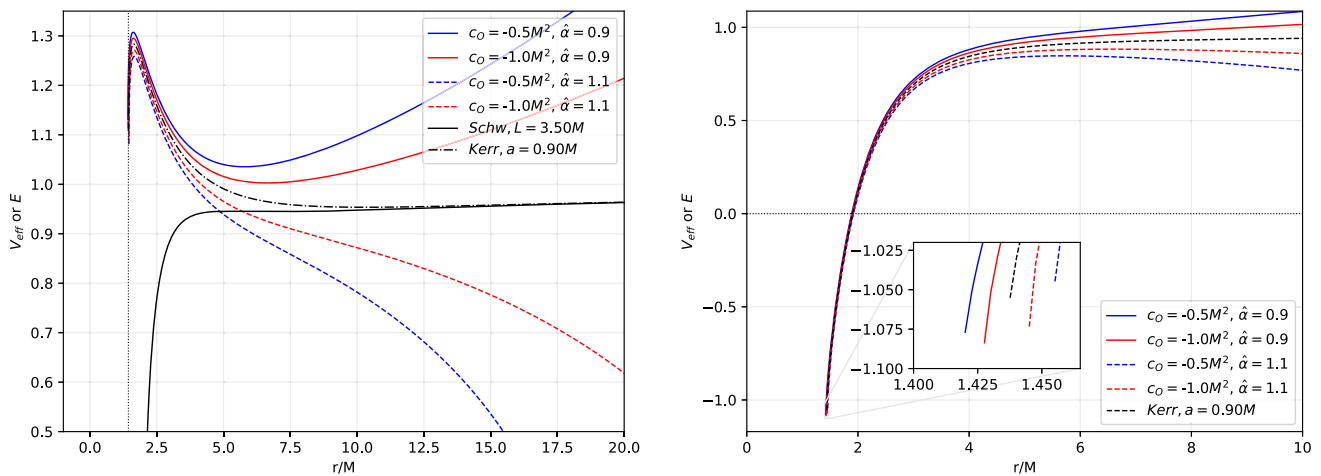
Fig. 6 The effective potential as a function of r/M for $L > 0$ (left-panel) and $L < 0$ (right-panel). In both plots, the black hole spin parameter is set to $a = 0.90M$

where $B = -8a^2 + r\left(r\Delta_r'' - 5\Delta_r'\right) + 8\Delta_r$. The ISCO radius can then be found by solving the Eq. [127]

$$
\eta(r)_{\text{isco}} = \pm 2\Delta_r\left(a^2 - \Delta_r\right)^2 \pm \frac{9}{4}r\Delta_r\left(a^2 - \Delta_r\right)\Delta_r'
$$

$$
\pm \frac{1}{16}r^3\Delta_r'\left(\Delta_r\Delta_r'' - 2\Delta_r'^2\right)
$$

$$
\pm \frac{1}{16}r^2\left[4\Delta_r\left(a^2 - \Delta_r\right)\Delta_r'' + \left(15\Delta_r - 4a^2\right)\Delta_r'^2\right]
$$

$$
+ a\Delta_r\sqrt{4a^2 + 2r\Delta_r' - 4\Delta_r}
$$

$$
\times \left[-a^2 + \frac{1}{8}r\left(r\Delta_r'' - 5\Delta_r'\right) + \Delta_r\right] = 0 \quad (60)
$$

which redues to the Kerr case

$$
3a^2 \mp 8a\sqrt{m}\sqrt{r} + r(6m - r) = 0 \quad (61)
$$

when $\Delta(r) = r^2 - 2mr + a^2$. The upper and lower signs in Eq. (60) correspond to the prograde and retrograde orbit of the massive particle at the ISCO radius, respectively. We determine ISCO radius numerically by plotting Eq. (60) in Fig. 7. First, we note that in the Schwarzschild case, the ISCO radius is located at $r = 6M$. For the extreme Kerr case, on the other hand, the prograde ISCO is at $r = M$ (which coincides with the prograde photonsphere) and retrograde ISCO is at $r = 9M$. Thus, in Fig. 7, the left-panel represents the retrograde ISCO where we can see clearly how the symmergent parameters affect the radius. The innermost radius, which determines the accretion disk's innermost region, is smaller in the AdS type whilst the dS type is slightly larger in the Kerr case. We note that the first root of η_{isco} is unphysical since those radii are smaller than the photonsphere in the retrograde case. Finally, we see the same symmergent effects in the prograde ISCO (right-panel of Fig. 7). Before we close this section, we remark that we used lower values of c_0 in time-like geodesics than when analyzing the null boundaries and geodesics. Thus, there must be some different constraints

to be considered in studying time-like geodesics. If we used the same parameters for the null case, the results would be unphysical. Nonetheless, even if c_0 are more negative, we see that time-like particles are more sensitive to symmergent effects.

5 Weak deflection angle from rotating symmergent black holes using Gauss–Bonnet theorem

In this section, we investigate the deflection angle of light rays from the rotating symmergent black hole in the weak field limit using the methodology given in [29,31]. Below, we briefly discuss the finite distance method. First of all, the deflection angle is defined as

$$
\hat{\theta} = \Psi_R - \Psi_S + \phi_{RS} \quad (62)
$$

in which ϕ_{RS} is the longitude separation angle, Ψ_R is the angle between light rays and radial direction, and Ψ_S is the angle between the observer and the source. Unit tangential vector e^i is used to write the above angle as follows

$$
(e^r, e^\theta, e^\phi) = \epsilon\left(\frac{dr}{d\phi}, 0, 1\right) \quad (63)
$$

where ϵ is a radial quantity. For a stationary spacetime described by the metric

$$
ds^2 = -A(r,\theta)dt^2 + B(r,\theta)dr^2 + C(r,\theta)d\theta^2
$$

$$
+ D(r,\theta)d\phi^2 - 2H(r,\theta)dtd\phi, \quad (64)
$$

one straightforwardly finds

$$
\epsilon = \frac{A(r)D(r) + H^2(r)}{A(r)(H(r) + A(r)b)}, \quad (65)
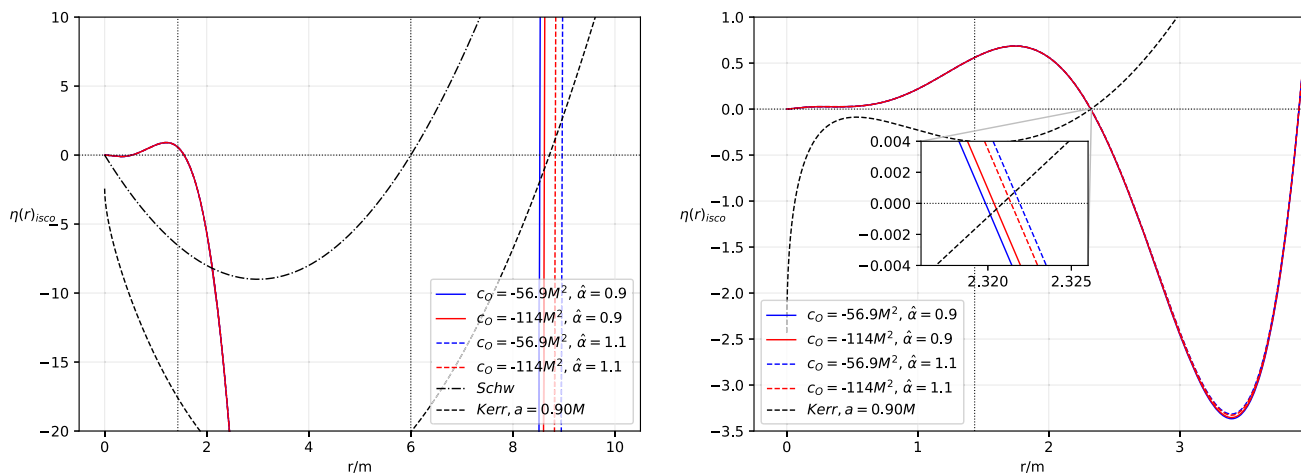$$

Fig. 7 Location of ISCO radius for counter-rotation of a massive particle (left-panel) and co-rotation of a massive particle (right-panel). We set $a = 0.90M$ in both panels

where b is the impact parameter. We can write conserved quantities energy and the angular momentum per unit mass in the form

$$E = A(r)\dot{t} + H(r)\dot{\phi} \qquad L = D(r)\dot{\phi} - H(r)\dot{t}, \tag{66}$$

where the overdot denotes the derivative of the coordinates t and ϕ with respect to the affine parameter λ (proper time). In the equatorial plane ($\theta = \frac{\pi}{2}$), the line element reduces to

$$dl^2 \equiv \gamma_{ij} dx^i dx^j \tag{67}$$

with the spatial metric γ_{ij}. It is then possible to define

$$\cos \Psi \equiv \gamma_{ij} e^i R^j. \tag{68}$$

as the angle between the direction e^i and the radial vector $R^j = (\frac{1}{\sqrt{\gamma_{rr}}}, 0, 0)$. Having $\cos \Psi$ at hand, we use equations (63) and (68) to get

$$\sin \Psi = \frac{H(r) + A(r)b}{\sqrt{A(r)D(r) + H^2(r)}}. \tag{69}$$

Now, using this methodology we can calculate the deflection angle of the symmergent black hole in the weak field limit. Indeed, with the impact parameter $b = \frac{L}{E}$ and radial coordinate $1/u$ in place of r we get

$$\left(\frac{du}{d\phi}\right)^2 = \frac{1}{b^2} - \frac{4aMu}{b^3} - u^2 + 2Mu^3 + \frac{1-\hat{\alpha}}{24\pi c_0}$$
$$- \frac{2a}{3b^3 u^2} \frac{(1-\hat{\alpha})}{8\pi c_0} - \frac{8aM}{3b^3 u} \frac{(1-\hat{\alpha})}{8\pi c_0}$$
$$+ \mathcal{O}\left[M^2, \left(\frac{1-\hat{\alpha}}{8\pi c_0}\right)^2, a^2\right] \tag{70}$$

where we considered only the retrograde solution. For the prograde solution, we just flip the sign of the spin parameter a. It is convenient to start by computing the separation angle

integral. This can be done by writing $\left(\frac{du}{d\phi}\right)^2 = F(u)$ and extracting the angle

$$\phi_{RS} = \int_S^R d\phi = \int_{u_S}^{u_0} \frac{1}{\sqrt{F(u)}} du + \int_{u_R}^{u_0} \frac{1}{\sqrt{F(u)}} du, \tag{71}$$

where u_S (u_R) is inverse distance to the source (observer), and u_0 is the inverse of the closest approach r_0. Considering the weak field and slow rotation approximations, the impact parameter can be related to u_0 as

$$b = \frac{1}{u_0} + M - 2aMu_0 + \mathcal{O}\left[M^2, \left(\frac{1-\hat{\alpha}}{8\pi c_0}\right)^2, a^2\right]. \tag{72}$$

Then, performing the necessary calculations we find

$$\phi_{RS} = \phi_{RS}^{Kerr} + \left(\frac{u_R}{\sqrt{1 - b^2 u_R^2}} + \frac{u_S}{\sqrt{1 - b^2 u_S^2}}\right) \frac{b^3}{6} \frac{(1-\hat{\alpha})}{8\pi c_0}$$
$$+ \left(\frac{b(2 - 3b^2 u_R^2)}{2(1 - b^2 u_R^2)^{3/2}} + \frac{b(2 - 3b^2 u_S^2)}{2(1 - b^2 u_S^2)^{3/2}}\right) \frac{M}{3} \frac{(1-\hat{\alpha})}{8\pi c_0}$$
$$+ \left(\frac{1 - 2b^2 u_R^2}{u_R\sqrt{1 - b^2 u_R^2}} + \frac{1 - 2b^2 u_S^2}{u_S\sqrt{1 - b^2 u_S^2}}\right) \frac{a}{3} \frac{(1-\hat{\alpha})}{8\pi c_0}$$
$$+ \mathcal{O}\left[M^2, \left(\frac{1-\hat{\alpha}}{8\pi c_0}\right)^2, a^2\right], \tag{73}$$

where the Kerr term is given by

$$\phi_{RS}^{Kerr} = \phi_{RS}^{SW} - \left(\frac{1}{\sqrt{1 - b^2 u_R^2}} + \frac{1}{\sqrt{1 - b^2 u_S^2}}\right) \frac{2aM}{b^2}. \tag{74}$$

In this equation, the Schwarzschild term is

$$\phi_{RS}^{Schw} = \pi - \arcsin(bu_R) - \arcsin(bu_S)$$

$$+\left(\frac{2-b^2u_R^2}{\sqrt{1-b^2u_R^2}}+\frac{2-b^2u_S^2}{\sqrt{1-b^2u_S^2}}\right)\frac{M}{b}. \qquad (75)$$

To get the remaining terms appearing in the light deflection angle expression, one should identify the Ψ terms. We find

$$\sin\Psi = bu - bMu^2 + 2aMu^2$$
$$-\left(\frac{bM}{6}-\frac{a}{3u}+\frac{b}{6u}\right)\frac{(1-\hat{\alpha})}{8\pi c_0}$$
$$+\mathcal{O}\left[M^2,\left(\frac{1-\hat{\alpha}}{8\pi c_0}\right)^2,a^2\right]. \qquad (76)$$

This relation produces

$$\Psi_R-\Psi_S = \Psi_R^{Kerr} - \left(\frac{1}{u_R\sqrt{1-b^2u_R^2}}+\frac{1}{u_S\sqrt{1-b^2u_S^2}}\right)$$
$$\times\frac{b}{6}\frac{(1-\hat{\alpha})}{8\pi c_0} - \left(\frac{2b^2u_R^2-1}{(1-b^2u_R^2)^{3/2}}+\frac{2b^2u_S^2-1}{(1-b^2u_S^2)^{3/2}}\right)$$
$$\times\frac{bM}{6}\frac{(1-\hat{\alpha})}{8\pi c_0}$$
$$+\left(\frac{1}{u_R\sqrt{1-b^2u_R^2}}+\frac{1}{u_S\sqrt{1-b^2u_S^2}}\right)\frac{a}{3}\frac{(1-\hat{\alpha})}{8\pi c_0}$$
$$+\mathcal{O}\left[M^2,\left(\frac{1-\hat{\alpha}}{8\pi c_0}\right)^2,a^2\right], \qquad (77)$$

where one has

$$\Psi_R^{Kerr}-\Psi_S^{Kerr} = \Psi_R^{Schw}-\Psi_R^{Schw}$$
$$+\left(\frac{u_R^2}{\sqrt{1-b^2u_R^2}}+\frac{u_S^2}{\sqrt{1-b^2u_S^2}}\right)2aM, \qquad (78)$$

and where one has found

$$\Psi_R^{Schw}-\Psi_R^{Schw} = (\arcsin(bu_R)+\arcsin(bu_S)-\pi)$$
$$-\left(\frac{u_R^2}{\sqrt{1-b^2u_R^2}}+\frac{u_S^2}{\sqrt{1-b^2u_S^2}}\right)Mb. \qquad (79)$$

Combining the above equations, we get an expression of the light deflection angle given by

$$\hat{\theta} = \left(\sqrt{1-b^2u_R^2}+\sqrt{1-b^2u_S^2}\right)\frac{2M}{b}$$
$$-\left(\sqrt{1-b^2u_R^2}-\sqrt{1-b^2u_S^2}\right)\frac{2aM}{b^2}$$
$$-\left(\frac{1-b^2u_R^2}{u_R\sqrt{1-b^2u_R^2}}+\frac{1-b^2u_S^2}{u_S\sqrt{1-b^2u_S^2}}\right)\frac{b}{6}\frac{(1-\hat{\alpha})}{8\pi c_0}$$
$$+\left(\frac{1}{\sqrt{1-b^2u_R^2}}+\frac{1}{\sqrt{1-b^2u_S^2}}\right)\frac{bM}{6}\frac{(1-\hat{\alpha})}{8\pi c_0}$$

$$+\left(\frac{\sqrt{1-b^2u_R^2}}{u_R}+\frac{\sqrt{1-b^2u_S^2}}{u_S}\right)\frac{2a}{3}\frac{(1-\hat{\alpha})}{8\pi c_0}$$
$$+\mathcal{O}\left[M^2,\left(\frac{1-\hat{\alpha}}{8\pi c_0}\right)^2,a^2\right]. \qquad (80)$$

This form can be reduced to a simplified one using certain convenable approximations. Taking $u_S b << 1$ and $u_R b << 1$, we can get an expression involving divergent terms coupled to the cosmological contributions. These terms should be existed to show the cosmological background dependence. The desired deflection angle of light rays is found to be

$$\hat{\theta} = \frac{4M}{b}-\frac{4aM}{b^2}+\frac{bM}{3}\frac{(1-\hat{\alpha})}{8\pi c_0}-\left(\frac{1}{u_R}+\frac{1}{u_S}\right)\frac{b}{6}\frac{(1-\hat{\alpha})}{8\pi c_0}$$
$$+\left(\frac{1}{u_R}+\frac{1}{u_S}\right)\frac{2a}{3}\frac{(1-\hat{\alpha})}{8\pi c_0}+\mathcal{O}\left[M^2,\left(\frac{1-\hat{\alpha}}{8\pi c_0}\right)^2,a^2\right]. \qquad (81)$$

An examination shows that this expression recovers many previous findings. Without the cosmological contributions, we get the results of the ordinary Symmergent black hole solutions investigated in [9].

Plotted in Fig. 8 are the Eqs. (80) (left-panel) and (81) (right-panel). The solid curves represent photons co-rotating with the black hole, while the dashed curves represent the counter-rotating photons. For the left-panel, which holds for finite distance, the results show that the co-rotating photons produce weak deflection angle at lower impact parameters compared to the counter-rotating photons. If we compare $\hat{\theta}$ for a specific orbital direction of photons, we see that the symmergent AdS type gives a higher value for $\hat{\theta}$ at large impact parameters. However, AdS type in the counter-rotation case gives a higher $\hat{\theta}$ than the co-rotation case. Finally, the right-panel stands for the case where we used the large distance approximation. Since the symmergent parameters are scaled, the location of the receiver in this case is comparable to the cosmic horizon. In this case, the symmergent effect is strong, giving the effects shown in the plot. We could see that there are cases where $\hat{\theta}$ is repulsive. In general, weak deflection angle is seen to have a strong sensitivity to the symmergent parameters.

5.1 Particle acceleration near rotating symmergent black hole backgrounds

As Banados, Silk and West (BSW) show that collisions in equatorial plane near a Kerr black hole can occur with an arbitrarily high center of mass-energy and Kerr black holes can serve as particle accelerators [128]. Then the BSW mechanism has been studied different black hole spacetimes [129–135]. In the present work, we find that the symmergent parameter c_0 has an important effect on the result. To do
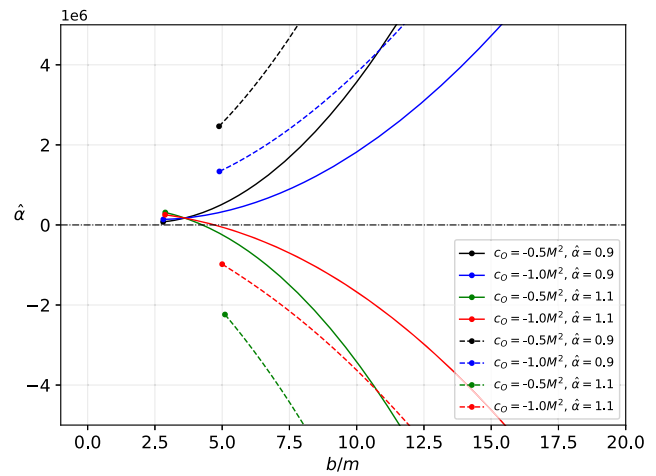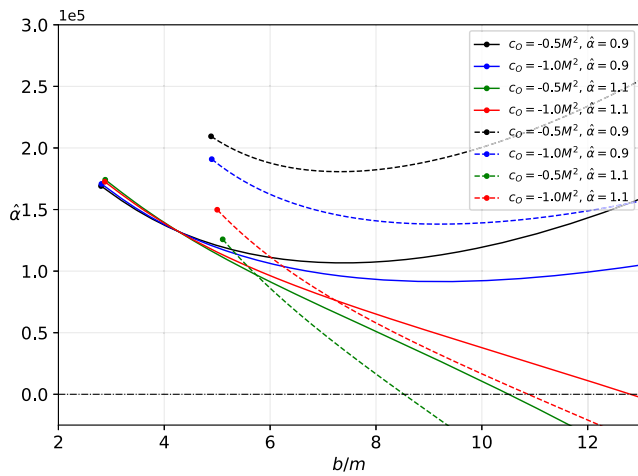
Fig. 8 Weak deflection angle of photons as a function of b/m for various values of the spin and symmergent parameters. The solid lines correspond to $a > 0$ (prograde) and dashed lines correspond to $a < 0$

(retrograde). In making these plots we take $u_S = u_R = 0.5b^{-1}$ (left), $u_S = u_R = 0.01b^{-1}$ (right), and $\hat{\alpha} = 0.90$. The horizontal dotted lines represent critical impact parameters in each case

that first we consider the particle motion on the equatorial plane ($\theta = \frac{\pi}{2}$, $\rho^2 = r^2$). In fact, generalized momenta P_μ can be written as ($\mu, \nu = t, r, \phi, \theta$)

$$P_\mu = g_{\mu\nu}\dot{x}^\nu \qquad (82)$$

where the dot stands for derivative with respect to the affine parameter λ. Then, one can write the generalized momenta P_t (test particle's energy per unit mass E) and P_ϕ (the angular momentum per unit mass L parallel to the symmetry axis)

$$P_t = g_{tt}\dot{t} + g_{t\phi}\dot{\phi}, \qquad (83)$$
$$P_\phi = g_{\phi\phi}\dot{\phi} + g_{t\phi}\dot{t} \qquad (84)$$

where one keeps in mind that P_t and P_ϕ are constants of motion.

Our goal is to study the CM energy of the two-particle collision in the background spacetime of the rotating symmergent black holes. To this end, we start with the CM energy E_{CM} [128]

$$E_{CM}^2 = 2m_0^2 \left(1 - g_{\mu\nu}u_1^\mu u_2^\nu\right) \qquad (85)$$

in which u_1^μ, u_2^ν are the 4-velocity vectors of the two particles ($u = (\dot{t}, \dot{r}, 0, \dot{\phi})$). Correspondingly, particle $i = 1, 2$ has angular momentum per unit mass L_i and energy per unit mass E_i. We also consider particles with the same rest mass m_0. Initially the two particles are at rest at infinity ($E_1/m_0 = 1$ and $E_2/m_0 = 1$) and then they approach the black hole and collide at a distance r. Then, their CM energy takes the form

$$E_{CM}^2 = \frac{2m_0^2}{\Delta_r r^2} \left[\left(r^2 + a^2\right)^2 - a\left(L_1 + L_2\right)\left(r^2 + a^2 - \Delta_r\right) \right.$$
$$\left. + L_1 L_2 \left(a^2 - \Delta_r\right) + \Delta_r \left(r^2 - a^2\right) - X_1 X_2 \right] \qquad (86)$$

with the functions

$$X_i = \sqrt{\left(aL_i - r^2 - a^2\right)^2 - \Delta_r \left(\left(L_i - a\right)^2 + \mu^2 r^2\right)}. \quad (87)$$

Collisions occur at the horizon of the black hole so that $\Delta_r = 0$ in Eq. (86) so that CM energy could diverge when the particles approach the horizon. It is not difficult to see that the denominator of E_{CM}^2 is zero there. Evidently, the maximal energy of the collision occurs if L_1 and L_2 are opposite (such as head-on collision). Plotted in Fig. 9 is E_{CM} as a function of the radial distance r. As is seen from the figure, CM energy blows up at the horizons. It demonstrates the radial dependence of the CM energy of the particles moving along circular orbits with the different symmergent parameters. The symmergent parameter decreases the CM energy.

6 Conclusion

In this paper, we have studied rotating black holes in symmergent gravity, and used deviations from the Kerr black hole to constrain the parameters of the symmergent gravity. Symmergent gravity generates parameters of the gravitational sector from flat spacetime loops. It induces the gravitational constant G and quadratic-curvature coefficient c_O. In the limit in which all fields are degenerate in mass, the vacuum energy V_O can be expressed in terms of G and c_O. We parametrize deviation from this degenerate limit by the parameter $\hat{\alpha}$. The black hole spacetime is dS for $\hat{\alpha} < 1$ and AdS for $\hat{\alpha} > 1$. In constraining the symmergent parameters c_O and $\hat{\alpha}$, we utilize the EHT observations on the M87* and Sgr. A* black holes.

We have analyzed symmergent gravity parameters for different spinning black hole properties. We first investigated the
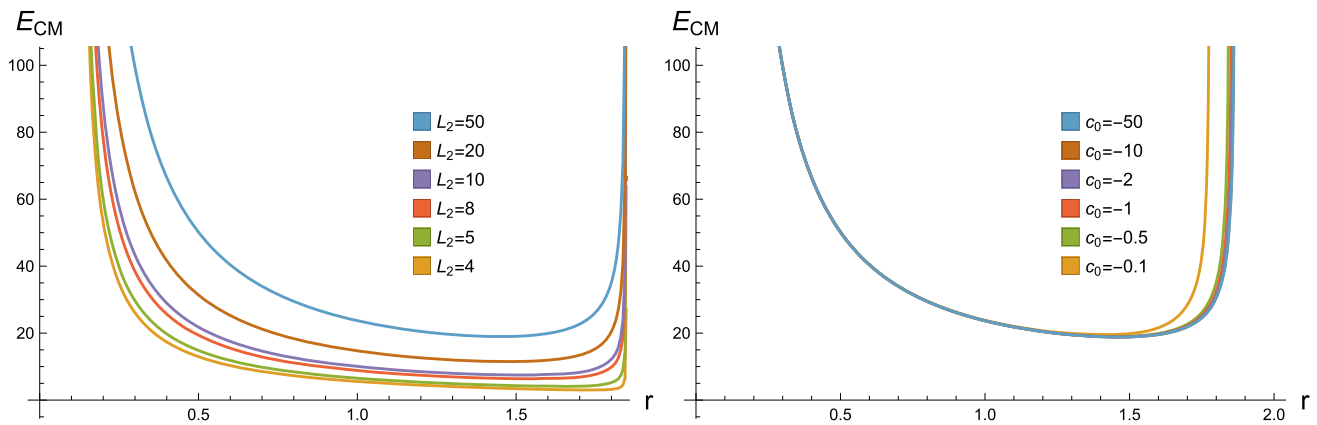
Fig. 9 Dependence of the CM energy E_{CM} on the radial distance r for different values of the spin and symmergent parameters. We consider two parameter sets $m = M = 1$, $L_1 = -4$, $c_0 = -0.5$, $\hat{\alpha} = 0.9$ and $a = 0.5$ (left-panel) as well as $m = M = 1$, $L_1 = -4$, $L_2 = 50$, $\hat{\alpha} = 0.9$ and $a = 0.5$ (right-panel). It is clear that the CM energy blows up at the horizons

effects of symmergent gravity on the photonsphere, black hole shadow, and certain observables related to them. Our findings show that location of the photonsphere depends on the symmergent effects due to its coupling to the black hole spin parameter. We have seen how the instability of the photon radii depends on and gets affected by c_O and $\hat{\alpha}$. Also, symmergent gravity effect is evident, even for observers deviating from the equatorial plane. Interesting effects are also seen in the energy emission rate, which may directly affect the black hole's lifetime. Constraints on symmergent parameters from the shadow radius data coming from recent observations are also discussed. For a low and high spin parameter a values (the parameter $\hat{\alpha}$ dictates whether the symmergent effect mimics the dS and AdS type), we found that the parameter c_0 fits within $\pm 2\sigma$ at 95% confidence level for M87* than in Sgr. A*. It means that the true value is somewhere within such confidence level. The plot in Fig. 5 reveals that the detection of symmergent effects can be achieved more easily in M87* than in Sgr. A*, for the obvious reason that the farther the galaxy is the stronger the symmergent effects are. Finally, for comparison, we also briefly analyzed such an effect on the time-like geodesic. Our findings indicate that massive particles are more sensitive to deviations caused by the symmergent parameter than null particles.

In addition, we investigated the symmergent effects on photons' weak deflection angle as they traverse near the black hole. We also considered the finite distance effects. We have found that the deflection angle depends on $\hat{\alpha}$ but the deviations are also caused by how far the receiver is from the black hole. This effect is clearly shown in Fig. 8. It implies that the weak deflection angle can detect symmergent effects more easily for black holes that are significantly remote compared to our location.

Lastly, we study the particle collision near the rotating symmergent black hole background and we analyze the pos-

sibility that rotating symmergent black holes could act as particle accelerators. We show that rotating symmergent black holes can serve as particle accelerators because the center-of-mass energies blow up at the horizons. As a result, the BSW mechanism depends on the value of the Symmergent parameter c_0 of the black hole.

Future research direction may include investigation of the shadow, and showing its dependence on the observer's state. One may also study the spherical photon orbits or the stability of time-like orbits.

References

1. D. Demir, Emergent Gravity as the eraser of anomalous gauge Boson masses, and QFT-GR concord. Gen. Relativ. Gravit. **53**, 22 (2021). https://doi.org/10.1007/s10714-021-02797-0. arXiv:2101.12391 [gr-qc]

2. D. Demir, S. Gravity, Seesawic New physics, and their experimental signatures. Adv. High Energy Phys. **2019**, 4652048 (2019). https://doi.org/10.1155/2019/4652048. arXiv:1901.07244 [hep-ph]

3. D.A. Demir, Curvature-restored gauge invariance and ultraviolet naturalness. Adv. High Energy Phys. **2016**, 6727805 (2016). https://doi.org/10.1155/2016/6727805. arXiv:1605.00377 [hep-ph]

4. W. Philip, Anderson, plasmons, gauge invariance, and mass. Phys. Rev. **130**, 439–442 (1963). https://doi.org/10.1103/PhysRev.130.439

5. F. Englert, R. Brout, Broken symmetry and the mass of gauge vector mesons. Phys. Rev. Lett. **13**, 321–323 (1964). https://doi.org/10.1103/PhysRevLett.13.321

6. W. Peter, Higgs, broken symmetries and the masses of gauge bosons. Phys. Rev. Lett. **13**, 508–509 (1964). https://doi.org/10.1103/PhysRevLett.13.508

7. İİ Çimdiker, Starobinsky inflation in emergent gravity. Phys. Dark Univ. **30**, 100736 (2020). https://doi.org/10.1016/j.dark.2020.100736

8. İ Çimdiker, D. Demir, A. Övgün, Black hole shadow in symmergent gravity. Phys. Dark Univ. **34**, 100900 (2021). https://doi.org/10.1016/j.dark.2021.100900. arXiv:2110.11904 [gr-qc]

9. J. Rayimbaev, R.C. Pantig, A. Övgün, A. Abdujabbarov, D. Demir, Quasiperiodic oscillations, weak field lensing and shadow cast around black holes in symmergent gravity (2022). arXiv:2206.06599 [gr-qc]

10. R. Ali, R. Babar, Z. Akhtar, A. Övgün, Thermodynamics and logarithmic corrections of symmergent black holes. Results Phys. 106300 (2023). https://doi.org/10.1016/j.rinp.2023.106300

11. K.S. Virbhadra, G.F.R. Ellis, Schwarzschild black hole lensing. Phys. Rev. D **62**, 084003 (2000). https://doi.org/10.1103/PhysRevD.62.084003. arXiv:astro-ph/9904193

12. K.S. Virbhadra, G.F.R. Ellis, Gravitational lensing by naked singularities. Phys. Rev. D **65**, 103004 (2002). https://doi.org/10.1103/PhysRevD.65.103004

13. K.S. Virbhadra, D. Narasimha, S.M. Chitre, Role of the scalar field in gravitational lensing. Astron. Astrophys. **337**, 1–8 (1998). arXiv:astro-ph/9801174

14. K.S. Virbhadra, C.R. Keeton, Time delay and magnification centroid due to gravitational lensing by black holes and naked singularities. Phys. Rev. D **77**, 124014 (2008). https://doi.org/10.1103/PhysRevD.77.124014. arXiv:0710.2333 [gr-qc]

15. K.S. Virbhadra, Relativistic images of Schwarzschild black hole lensing. Phys. Rev. D **79**, 083004 (2009). https://doi.org/10.1103/PhysRevD.79.083004. arXiv:0810.2109 [gr-qc]

16. S.L. Adle, K.S. Virbhadra, Cosmological constant corrections to the photon sphere and black hole shadow radii (2022). arXiv:2205.04628 [gr-qc]

17. V. Bozza, S. Capozziello, G. Iovane, G. Scarpetta, Strong field limit of black hole gravitational lensing. Gen. Relativ. Gravit. **33**, 1535–1548 (2001). https://doi.org/10.1023/A:1012292927358. arXiv:gr-qc/0102068

18. V. Bozza, Gravitational lensing in the strong field limit. Phys. Rev. D **66**, 103001 (2002). https://doi.org/10.1103/PhysRevD.66.103001. arXiv:gr-qc/0208075

19. V. Perlick, On the exact gravitational lens equation in spherically symmetric and static space-times. Phys. Rev. D **69**, 064017 (2004). https://doi.org/10.1103/PhysRevD.69.064017. arXiv:gr-qc/0307072

20. G. He, X. Zhou, Z. Feng, M. Xueling, H. Wang, W. Li, C. Pan, W. Lin, Gravitational deflection of massive particles in Schwarzschild-de Sitter spacetime. Eur. Phys. J. C **80**, 835 (2020). https://doi.org/10.1140/epjc/s10052-020-8382-z

21. K.S. Virbhadra, Compactness of supermassive dark objects at galactic centers (2022). arXiv:2204.01792 [gr-qc]

22. K.S. Virbhadra, Distortions of images of Schwarzschild lensing (2022). arXiv:2204.01879 [gr-qc]

23. G.W. Gibbons, M.C. Werner, Applications of the Gauss–Bonnet theorem to gravitational lensing. Class. Quantum Gravity **25**, 235009 (2008). https://doi.org/10.1088/0264-9381/25/23/235009. arXiv:0807.0854 [gr-qc]

24. A. Övgün, Light deflection by Damour–Solodukhin wormholes and Gauss–Bonnet theorem. Phys. Rev. D **98**, 044033 (2018). https://doi.org/10.1103/PhysRevD.98.044033. arXiv:1805.06296 [gr-qc]

25. A. Övgün, Weak field deflection angle by regular black holes with cosmic strings using the Gauss–Bonnet theorem. Phys. Rev. D **99**, 104075 (2019). https://doi.org/10.1103/PhysRevD.99.104075. arXiv:1902.04411 [gr-qc]

26. A. Övgün, Deflection angle of photons through dark matter by black holes and wormholes using Gauss–Bonnet theorem. Universe **5**, 115 (2019). https://doi.org/10.3390/universe505115. arXiv:1806.05549 [physics.gen-ph]

27. W. Javed, R. Babar, A. Övgün, Effect of the dilaton field and plasma medium on deflection angle by black holes in Einstein–Maxwell-dilaton-axion theory. Phys. Rev. D **100**, 104032 (2019). https://doi.org/10.1103/PhysRevD.100.104032. arXiv:1910.11697 [gr-qc]

28. M.C. Werner, Gravitational lensing in the Kerr-Randers optical geometry. Gen. Relativ. Gravit. **44**, 3047–3057 (2012). https://doi.org/10.1007/s10714-012-1458-9. arXiv:1205.3876 [gr-qc]

29. A. Ishihara, Y. Suzuki, T. Ono, T. Kitamura, H. Asada, Gravitational bending angle of light for finite distance and the Gauss–Bonnet theorem. Phys. Rev. D **94**, 084015 (2016). https://doi.org/10.1103/PhysRevD.94.084015. arXiv:1604.08308 [gr-qc]

30. A. Ishihara, Y. Suzuki, T. Ono, H. Asada, Finite-distance corrections to the gravitational bending angle of light in the strong deflection limit. Phys. Rev. D **95**, 044017 (2017). https://doi.org/10.1103/PhysRevD.95.044017. arXiv:1612.04044 [gr-qc]

31. T. Ono, A. Ishihara, H. Asada, Gravitomagnetic bending angle of light with finite-distance corrections in stationary axisymmetric spacetimes. Phys. Rev. D **96**, 104037 (2017). https://doi.org/10.1103/PhysRevD.96.104037. arXiv:1704.05615 [gr-qc]

32. Z. Li, A. Övgün, Finite-distance gravitational deflection of massive particles by a Kerr-like black hole in the bumblebee gravity model. Phys. Rev. D **101**, 024040 (2020). https://doi.org/10.1103/PhysRevD.101.024040. arXiv:2001.02074 [gr-qc]

33. Z. Li, G. Zhang, A. Övgün, Circular orbit of a particle and weak gravitational lensing. Phys. Rev. D **101**, 124058 (2020). https://doi.org/10.1103/PhysRevD.101.124058. arXiv:2006.13047 [gr-qc]

34. A. Belhaj, H. Belmahi, M. Benali, H. Moumni El, Light Deflection by Rotating Regular Black Holes with a Cosmological Constant (2022). arXiv:2204.10150 [gr-qc]

35. W. Javed, M. Atique, R.C. Pantig, A. Övgün, Weak deflection angle Hawking radiation and greybody bound of Reissner–Nordström black hole corrected by bounce parameter. Symmetry **15**, 148 (2023). https://doi.org/10.3390/sym15010148. arXiv:2301.01855 [gr-qc]

36. W. Javed, M. Atique, R.C. Pantig, A. Övgün, Weak lensing, Hawking radiation and greybody factor bound by a charged black holes with non-linear electrodynamics corrections. Int. J. Geom. Meth-

ods Mod. Phys. **96**, 2350040 (2022). https://doi.org/10.1142/s0219887823500408

37. R.C. Pantig, A. Övgün, Testing dynamical torsion effects on the charged black hole's shadow, deflection angle and greybody with M87* and Sgr. A* from EHT. Ann. Phys. **448**, 169197 (2023). https://doi.org/10.1016/j.aop.2022.169197. arXiv:2206.02161 [gr-qc]

38. S. Vagnozzi, R. Roy, Y.-D. Tsai, L. Visinelli, Horizon-scale tests of gravity theories and fundamental physics from the Event Horizon Telescope image of Sagittarius A* (2022). arXiv:2205.07787 [gr-qc]

39. Y. Chen, R. Roy, S. Vagnozzi, L. Visinelli, Superradiant evolution of the shadow and photon ring of Sgr A⋆ (2022). arXiv:2205.06238 [astro-ph.HE]

40. I. Dymnikova, K. Kraav, Identification of a regular black hole by its shadow. Universe **5**, 1–16 (2019). https://doi.org/10.3390/universe5070163

41. R.C. Pantig, A. Övgün, Dehnen halo effect on a black hole in an ultra-faint dwarf galaxy. JCAP **08**, 056 (2022). https://doi.org/10.1088/1475-7516/2022/08/056. arXiv:2202.07404 [astro-ph.GA]

42. A. Uniyal, R.C. Pantig, A. Övgün, Probing a non-linear electrodynamics black hole with thin accretion disk, shadow, and deflection angle with M87* and Sgr A* from EHT. Phys. Dark Univ. **40**, 101178 (2023). https://doi.org/10.1016/j.dark.2023.101178. arXiv:2205.11072 [gr-qc]

43. Xi.-M. Kuang, A. Övgün, Strong gravitational lensing and shadow constraint from M87* of slowly rotating Kerr-like black hole (2022). arXiv:2205.11003 [gr-qc]

44. Y. Meng, X.-M. Kuang, Z.-Y. Tang, Photon regions, shadow observables and constraints from M87* of a charged rotating black hole (2022). arXiv:2204.00897 [gr-qc]

45. Z.-Y. Tang, X.-M. Kuang, B. Wang, W.-L. Qian, The length of a compact extra dimension from shadow (2022). arXiv:2206.08608 [gr-qc]

46. X.-M. Kuang, Z.-Y. Tang, B. Wang, A. Wang, Constraining a modified gravity theory in strong gravitational lensing and black hole shadow observations (2022). arXiv:2206.05878 [gr-qc]

47. S.-W. Wei, Y.-C. Zou, Y.-X. Liu, R.B. Mann, Curvature radius and Kerr black hole shadow. JCAP **08**, 030 (2019). https://doi.org/10.1088/1475-7516/2019/08/030. arXiv:1904.07710 [gr-qc]

48. X. Zhaoyi, X. Hou, J. Wang, Possibility of identifying matter around rotating black hole with black hole shadow. JCAP **10**, 046 (2018). https://doi.org/10.1088/1475-7516/2018/10/046. arXiv:1806.09415 [gr-qc]

49. X. Hou, X. Zhaoyi, J. Wang, Rotating black hole shadow in perfect fluid dark matter. JCAP **12**, 040 (2018). https://doi.org/10.1088/1475-7516/2018/12/040. arXiv:1810.06381 [gr-qc]

50. C. Bambi, K. Freese, S. Vagnozzi, L. Visinelli, Testing the rotational nature of the supermassive object M87* from the circularity and size of its first image. Phys. Rev. D **100**, 044057 (2019). https://doi.org/10.1103/PhysRevD.100.044057. arXiv:1904.12983 [gr-qc]

51. N. Tsukamoto, Black hole shadow in an asymptotically-flat, stationary, and axisymmetric spacetime: the Kerr–Newman and rotating regular black holes. Phys. Rev. D **97**, 064021 (2018). https://doi.org/10.1103/PhysRevD.97.064021. arXiv:1708.07427 [gr-qc]

52. R. Kumar, S.G. Ghosh, A. Wang, Gravitational deflection of light and shadow cast by rotating Kalb–Ramond black holes. Phys. Rev. D **101**, 104001 (2020). https://doi.org/10.1103/PhysRevD.101.104001. arXiv:2001.00460 [gr-qc]

53. R. Kumar, S.G. Ghosh, A. Wang, Shadow cast and deflection of light by charged rotating regular black holes. Phys. Rev. D **100**, 1–32 (2019). https://doi.org/10.1103/PhysRevD.100.124024. arXiv:1912.05154

54. M. Wang, S. Chen, J. Jing, Shadow casted by a Konoplya-Zhidenko rotating non-Kerr black hole. J. Cosmol. Astropart. Phys. **2017**, 1–14 (2017). https://doi.org/10.1088/1475-7516/2017/10/051. arXiv:1707.09451

55. M. Wang, S. Chen, J. Jing, Chaotic shadow of a non-Kerr rotating compact object with quadrupole mass moment. Phys. Rev. D **98**, 1–22 (2018). https://doi.org/10.1103/PhysRevD.98.104040. arXiv:1801.02118

56. L. Amarilla, E.F. Eiroa, Shadows of rotating black holes in alternative theories, *14th Marcel Grossman Meet. Recent Dev. Theor. Exp. Gen. Relativ. Astrophys. Relativ. F. Theor. Proc.*, (2018), p. 3543–3548. https://doi.org/10.1142/9789813226609_0459. arXiv:1512.08956

57. H. Peng-Zhang, F. Qi-Qi, Z. Hao-Ran, D. Jian-Bo, Shadows of rotating Hayward-de Sitter black holes with astrometric observables. Eur. Phys. J. C **80**, 1195 (2020). https://doi.org/10.1140/epjc/s10052-020-08707-z

58. O.Y. Tsupko, Z. Fan, G.S. Bisnovatyi-Kogan, Black hole shadow as a standard ruler in cosmology. Class. Quantum Gravity **37**, 065016 (2020). https://doi.org/10.1088/1361-6382/ab6f7d. arXiv:1905.10509 [gr-qc]

59. K. Hioki, K. Maeda, Measurement of the Kerr Spin parameter by observation of a compact object's shadow. Phys. Rev. D **80**, 024042 (2009). https://doi.org/10.1103/PhysRevD.80.024042. arXiv:0904.3575 [astro-ph.HE]

60. R.A. Konoplya, Shadow of a black hole surrounded by dark matter. Phys. Lett. B **795**, 1–6 (2019). https://doi.org/10.1016/j.physletb.2019.05.043. arXiv:1905.00064 [gr-qc]

61. M. Okyay, A. Övgün, Nonlinear electrodynamics effects on the black hole shadow, deflection angle, quasinormal modes and greybody factors. JCAP **01**, 009 (2022). https://doi.org/10.1088/1475-7516/2022/01/009. arXiv:2108.07766 [gr-qc]

62. A. Belhaj, M. Benali, A. El Balali, H. El Moumni, S.E. Ennadifi, Deflection angle and shadow behaviors of quintessential black holes in arbitrary dimensions. Class. Quantum Gravity **37**, 215004 (2020). https://doi.org/10.1088/1361-6382/abbaa9. arXiv:2006.01078 [gr-qc]

63. P.-C. Li, M. Guo, B. Chen, Shadow of a Spinning Black Hole in an Expanding Universe. Phys. Rev. D **101**, 084041 (2020). https://doi.org/10.1103/PhysRevD.101.084041. arXiv:2001.04231 [gr-qc]

64. R. Ling, H. Guo, H. Liu, X.-M. Kuang, B. Wang, Shadow and near-horizon characteristics of the acoustic charged black hole in curved spacetime. Phys. Rev. D **104**, 104003 (2021). https://doi.org/10.1103/PhysRevD.104.104003. arXiv:2107.05171 [gr-qc]

65. A. Belhaj, H. Belmahi, M. Benali, W. El Hadri, H. El Moumni, E. Torrente-Lujan, Shadows of 5D black holes from string theory. Phys. Lett. B **812**, 136025 (2021). https://doi.org/10.1016/j.physletb.2020.136025. arXiv:2008.13478 [hep-th]

66. P.V.P. Cunha, C.A.R. Herdeiro, Shadows, and strong gravitational lensing: a brief review. Gen. Relativ. Gravit. **50**, 42 (2018). https://doi.org/10.1007/s10714-018-2361-9. arXiv:1801.00860 [gr-qc]

67. S.E. Gralla, D.E. Holz, R.M. Wald, Black hole shadows, photon rings, and lensing rings. Phys. Rev. D **100**, 024018 (2019). https://doi.org/10.1103/PhysRevD.100.024018. arXiv:1906.00873 [astro-ph.HE]

68. V. Perlick, O.Y. Tsupko, G.S. Bisnovatyi-Kogan, Influence of a plasma on the shadow of a spherically symmetric black hole. Phys. Rev. D **92**, 104031 (2015). https://doi.org/10.1103/PhysRevD.92.104031. arXiv:1507.04217 [gr-qc]

69. P.G. Nedkova, V.K. Tinchev, S.S. Yazadjiev, Shadow of a rotating traversable wormhole. Phys. Rev. D **88**, 124019 (2013). https://doi.org/10.1103/PhysRevD.88.124019. arXiv:1307.7647 [gr-qc]

70. Z. Li, C. Bambi, Measuring the Kerr spin parameter of regular black holes from their shadow. JCAP **01**, 041 (2014). https://doi.org/10.1088/1475-7516/2014/01/041. arXiv:1309.1606 [gr-qc]

71. M. Khodadi, G. Lambiase, D.F. Mota, No-hair theorem in the wake of Event Horizon Telescope. JCAP **09**, 028 (2021). https://doi.org/10.1088/1475-7516/2021/09/028. arXiv:2107.00834 [gr-qc]

72. M. Khodadi, G. Lambiase, Probing the Lorentz symmetry violation using the first image of Sagittarius A*: constraints on standard-model extension coefficients (2022). arXiv:2206.08601 [gr-qc]

73. P.V.P. Cunha, C.A.R. Herdeiro, B. Kleihaus, J. Kunz, E. Radu, Shadows of Einstein–dilaton–Gauss–Bonnet black holes. Phys. Lett. B **768**, 373–379 (2017). https://doi.org/10.1016/j.physletb.2017.03.020. arXiv:1701.00079 [gr-qc]

74. R. Shaikh, Black hole shadow in a general rotating spacetime obtained through Newman–Janis algorithm. Phys. Rev. D **100**, 024028 (2019). https://doi.org/10.1103/PhysRevD.100.024028. arXiv:1904.08322 [gr-qc]

75. A. Allahyari, M. Khodadi, S. Vagnozzi, D.F. Mota, Magnetically charged black holes from non-linear electrodynamics and the Event Horizon telescope. JCAP **02**, 003 (2020). https://doi.org/10.1088/1475-7516/2020/02/003. arXiv:1912.08231 [gr-qc]

76. A. Yumoto, D. Nitta, T. Chiba, N. Sugiyama, Shadows of multiblack holes: analytic exploration. Phys. Rev. D **86**, 103001 (2012). https://doi.org/10.1103/PhysRevD.86.103001. arXiv:1208.0635 [gr-qc]

77. P.V.P. Cunha, C.A.R. Herdeiro, E. Radu, H.F. Runarsson, Shadows of Kerr black holes with and without scalar hair. Int. J. Mod. Phys. D **25**, 1641021 (2016). https://doi.org/10.1142/S0218271816410212. arXiv:1605.08293 [gr-qc]

78. J.W. Moffat, Modified gravity black holes and their observable shadows. Eur. Phys. J. C **75**, 130 (2015). https://doi.org/10.1140/epjc/s10052-015-3352-6. arXiv:1502.01677 [gr-qc]

79. P.V.P. Cunha, J. Grover, C. Herdeiro, E. Radu, H. Runarsson, A. Wittig, Chaotic lensing around boson stars and Kerr black holes with scalar hair. Phys. Rev. D **94**, 104023 (2016). https://doi.org/10.1103/PhysRevD.94.104023. arXiv:1609.01340 [gr-qc]

80. F.A. Zakharov, Constraints on a charge in the Reissner–Nordström metric for the black hole at the Galactic Center. Phys. Rev. D **90**, 062007 (2014). https://doi.org/10.1103/PhysRevD.90.062007. arXiv:1407.7457 [gr-qc]

81. R.A. Hennigar, M.B.J. Poshteh, R.B. Mann, Shadows, signals, and stability in Einsteinian cubic gravity. Phys. Rev. D **97**, 064041 (2018). https://doi.org/10.1103/PhysRevD.97.064041. arXiv:1801.03223 [gr-qc]

82. L. Chakhchi, H. El Moumni, K. Masmar, Shadows and optical appearance of a power-Yang-Mills black hole surrounded by different accretion disk profiles. Phys. Rev. D **105**, 064031 (2022). https://doi.org/10.1103/PhysRevD.105.064031

83. R.C. Pantig, A. Övgün, Black hole in quantum wave dark matter. Fortsch. Phys. **2022**, 2200164 (2022). https://doi.org/10.1002/prop.202200164. arXiv:2210.00523 [gr-qc]

84. R.C. Pantig, L. Mastrototaro, G. Lambiase, A. Övgün, Shadow, lensing, quasinormal modes, greybody bounds and neutrino propagation by dyonic ModMax black holes. Eur. Phys. J. C **82**, 1155 (2022). https://doi.org/10.1140/epjc/s10052-022-11125-y. arXiv:2208.06664 [gr-qc]

85. N.J. Leo, S. Lobos, R.C. Pantig, Generalized extended uncertainty principle black holes: shadow and lensing in the macro- and microscopic realms. Physics **4**, 1318–1330 (2022). https://doi.org/10.3390/physics4040084

86. R.C. Pantig, A. Övgün, Dark matter effect on the weak deflection angle by black holes at the center of Milky Way and M87 galaxies. Eur. Phys. J. C **82**, 391 (2022). https://doi.org/10.1140/epjc/s10052-022-10319-8. arXiv:2201.03365 [gr-qc]

87. J.L. Synge, The escape of photons from gravitationally intense stars. Mon. Not. R. Astron. Soc. **131**, 463–466 (1966). https://doi.org/10.1093/mnras/131.3.463

88. J.P. Luminet, Image of a spherical black hole with thin accretion disk. Astron. Astrophys. **75**, 228–235 (1979)

89. J.M. Bardeen, Timelike and null geodesics in the Kerr metric, in *Booktitle Les Houches Summer School of Theoretical Physics: Black Holes* (1973), p. 215–240

90. S. Chandrasekhar, *The Mathematical Theory of Black Holes* (Oxford University Press, New York, 1998)

91. B.P. Abbott et al., (LIGO Scientific, Virgo), Observation of gravitational waves from a binary black hole merger. Phys. Rev. Lett. **116**, 061102 (2016). https://doi.org/10.1103/PhysRevLett.116.061102. arXiv:1602.03837 [gr-qc]

92. K. Akiyama et al. (Event Horizon Telescope), First M87 Event Horizon Telescope Results. VI. The shadow and mass of the central black hole. Astrophys. J. Lett. **875**, L6 (2019). https://doi.org/10.3847/2041-8213/ab1141. arXiv:1906.11243 [astro-ph.GA]

93. K. Akiyama et al., (Event Horizon Telescope), First Sagittarius A* Event horizon telescope results. I. The shadow of the supermassive black hole in the Center of the Milky Way. Astrophys. J. Lett. **930**, L12 (2022). https://doi.org/10.3847/2041-8213/ac6674

94. A. Macias, A. Camacho, On the incompatibility between quantum theory and general relativity. Phys. Lett. B **663**, 99–102 (2008). https://doi.org/10.1016/j.physletb.2008.03.052

95. R.M. Wald, The formulation of quantum field theory in curved spacetime. Einstein Stud. **14**, 439–449 (2018). https://doi.org/10.1007/978-1-4939-7708-6_15. arXiv:0907.0416 [gr-qc]

96. F. Dyson, Is a graviton detectable? Int. J. Mod. Phys. A **28**, 1330041 (2013). https://doi.org/10.1142/S0217751X1330041X

97. G. 't Hooft, M.J.G. Veltman, One loop divergencies in the theory of gravitation. Ann. Inst. H. Poincare Phys. Theor. A **20**, 69–94 (1974)

98. A.D. Sakharov, Vacuum quantum fluctuations in curved space and the theory of gravitation. Dokl. Akad. Nauk Ser. Fiz. **177**, 70–71 (1967). https://doi.org/10.1070/PU1991v034n05ABEH002498

99. M. Visser, Sakharov's induced gravity: a modern perspective. Mod. Phys. Lett. A **17**, 977–992 (2002). https://doi.org/10.1142/S0217732302006886. arXiv:gr-qc/0204062

100. E.P. Verlinde, Emergent gravity, the dark universe. SciPost Phys. **2**, 016 (2017). https://doi.org/10.21468/SciPostPhys.2.3.016. arXiv:1611.02269 [hep-th] https://doi.org/10.21468/SciPostPhys.2.3.016

101. C.D. Froggatt, H.B. Nielsen, Derivation of Poincare invariance from general quantum field theory. Ann. Phys. **517**, 115 (2005). https://doi.org/10.1002/andp.200410134. arXiv:hep-th/0501149

102. J. Polchinski, Renormalization and effective Lagrangians. Nucl. Phys. B **231**, 269–295 (1984). https://doi.org/10.1016/0550-3213(84)90287-6

103. H. Umezawa, J. Yukawa, E. Yamada, The problem of vacuum polarization. Prog. Theor. Phys. **3**, 317–318 (1948). https://doi.org/10.1143/ptp/3.3.317

104. G. Kallen, Higher approximations in the external field for the problem of vacuum polarization. Helv. Phys. Acta **22**, 637–654 (1949). https://doi.org/10.1007/978-3-319-00627-7_87

105. V. Vitagliano, T.P. Sotiriou, S. Liberati, The dynamics of metric-affine gravity. Ann. Phys. **326**, 1259–1273 (2011). https://doi.org/10.1016/j.aop.2011.02.008. (**Erratum: Annals Phys. 329, 186–187 (2013)**). arXiv:1008.0171 [gr-qc]

106. C.N. Karahan, A. Altas, D.A. Demir, Scalars, vectors and tensors from metric-affine gravity. Gen. Relativ. Gravit. **45**, 319–343 (2013). https://doi.org/10.1007/s10714-012-1473-x. arXiv:1110.5168 [gr-qc]

107. D. Demir, B. Puliçe, Geometric dark matter. JCAP **04**, 051 (2020). https://doi.org/10.1088/1475-7516/2020/04/051. arXiv:2001.06577 [hep-ph]

108. G. 't Hooft, Dimensional reduction in quantum gravity. Conf. Proc. C **930308**, 284–296 (1993). arXiv:gr-qc/9310026

109. A.G. Cohen, D.B. Kaplan, A.E. Nelson, Effective field theory, black holes, and the cosmological constant. Phys. Rev. Lett. **82**, 4971–4974 (1999). https://doi.org/10.1103/PhysRevLett.82.4971. arXiv:hep-th/9803132

110. N.D. Birrell, P.C.W. Davies, *Quantum Fields in Curved Space, Cambridge Monographs on Mathematical Physics* (Cambridge University Press, Cambridge, 1984). https://doi.org/10.1017/CBO9780511622632

111. J.A.R. Cembranos, A. de la Cruz-Dombriz, P. Jimeno Romero, Kerr-Newman black holes in $f(R)$ theories. Int. J. Geom. Methods Mod. Phys. **11**, 1450001 (2014). https://doi.org/10.1142/S0219887814500017. arXiv:1109.4519 [gr-qc]

112. S. Dastan, R. Saffari, S. Soroushfar, Shadow of a charged rotating black hole in f(R) gravity. Eur. Phys. J. Plus **137**, 1002 (2022). https://doi.org/10.1140/epjp/s13360-022-03218-0. arXiv:1606.06994 [gr-qc]

113. D. Perez, G.E. Romero, S.E.P. Bergliaffa, Accretion disks around black holes in modified strong gravity. Astron. Astrophys. **551**, A4 (2013). https://doi.org/10.1051/0004-6361/201220378. arXiv:1212.2640 [astro-ph.CO]

114. A.G. Suvorov, Gravitational perturbations of a Kerr black hole in $f(R)$ gravity. Phys. Rev. D **99**, 124026 (2019). https://doi.org/10.1103/PhysRevD.99.124026. arXiv:1905.02021 [gr-qc]

115. Y.S. Myung, Instability of a Kerr black hole in $f(R)$ gravity. Phys. Rev. D **88**, 104017 (2013). https://doi.org/10.1103/PhysRevD.88.104017. arXiv:1309.3346 [gr-qc]

116. G.L.L. Nashed, S. Nojiri, Rotating black hole in f(R) theory. JCAP **11**, 007 (2021). https://doi.org/10.1088/1475-7516/2021/11/007. arXiv:2109.02638 [gr-qc]

117. G.G.L. Nashed, New rotating AdS/dS black holes in $f(R)$ gravity. Phys. Lett. B **815**, 136133 (2021). https://doi.org/10.1016/j.physletb.2021.136133. arXiv:2102.11722 [gr-qc]

118. G.W. Gibbons, M.J. Perry, C.N. Pope, The first law of thermodynamics for Kerr-anti-de Sitter black holes. Class. Quantum Gravity **22**, 1503–1526 (2005). https://doi.org/10.1088/0264-9381/22/9/002. arXiv:hep-th/0408217

119. Z. Gao, X. Kong, L. Zhao, Thermodynamics of Kerr-AdS black holes in the restricted phase space. Eur. Phys. J. C **82**, 112 (2022). https://doi.org/10.1140/epjc/s10052-022-10080-y. arXiv:2112.08672 [hep-th]

120. L. Pogosian, A. Silvestri, The pattern of growth in viable f(R) cosmologies. Phys. Rev. D **77**, 023503 (2008) (**Erratum: Phys.Rev.D 81, 049901 (2010)**). arXiv:0709.0296 [astro-ph]

121. P. Slany, Z. Stuchlik, Equatorial circular orbits in Kerr–Newman-de Sitter spacetimes. Eur. Phys. J. C **80**, 587 (2020). https://doi.org/10.1140/epjc/s10052-020-8142-0

122. B. Carter, Global structure of the Kerr family of gravitational fields. Phys. Rev. **174**, 1559 (1968)

123. T. Johannsen, Photon rings around Kerr and Kerr-like black holes. Astrophys. J. **777**, 170 (2013). https://doi.org/10.1088/0004-637X/777/2/170

124. K. Akiyama et al. (Event Horizon Telescope), First M87 event horizon telescope results. I. The shadow of the supermassive black hole. Astrophys. J. Lett. **875**, L1 (2019). https://doi.org/10.3847/2041-8213/ab0ec7. arXiv:1906.11238 [astro-ph.GA]

125. B. Bautista-Olvera, J.C. Degollado, G. German, Geodesic structure of a rotating regular black hole, 1–18 (2019). arXiv:1908.01886

126. P. Slaný, M. Pokorná, Z. Stuchlík, Equatorial circular orbits in Kerr-anti-de Sitter spacetimes. Gen. Relativ. Gravit. **45**, 2611–2633 (2013). https://doi.org/10.1007/s10714-013-1606-x. arXiv:0307049 [gr-qc]

127. R.C. Pantig, E.T. Rodulfo, Rotating dirty black hole and its shadow. Chin. J. Phys. **68**, 236–257 (2020). https://doi.org/10.1016/j.cjph.2020.08.001. arXiv:2003.06829 [gr-qc]

128. M. Banados, J. Silk, S.M. West, Kerr black holes as particle accelerators to arbitrarily high energy. Phys. Rev. Lett. **103**, 111102 (2009). https://doi.org/10.1103/PhysRevLett.103.111102. arXiv:0909.0169 [hep-ph]

129. M. Halilsoy, A. Ovgun, Particle collision near 1 + 1-dimensional Horava–Lifshitz black hole and naked singularity. Adv. High Energy Phys. **2017**, 4383617 (2017). https://doi.org/10.1155/2017/4383617. arXiv:1504.03840 [gr-qc]

130. M. Halilsoy, A. Ovgun, Particle acceleration by static black holes in a model of $f(R)$ gravity. Can. J. Phys. **95**, 1037–1041 (2017). https://doi.org/10.1139/cjp-2017-0138. arXiv:1507.00633 [gr-qc]

131. J. Yang, Y.-L. Li, Y. Li, S.-W. Wei, Y.-X. Liu, Particle collisions in the lower dimensional rotating black hole space-time with the cosmological constant. Adv. High Energy Phys. **2014**, 204016 (2014). https://doi.org/10.1155/2014/204016. arXiv:1202.4159 [hep-th]

132. Y. Li, J. Yang, Y.-L. Li, S.-W. Wei, Y.-X. Liu, Particle acceleration in Kerr-(anti-) de Sitter black hole backgrounds. Class. Quantum Gravity **28**, 225006 (2011). https://doi.org/10.1088/0264-9381/28/22/225006. arXiv:1012.0748 [hep-th]

133. S. Zhang, Y. Liu, X. Zhang, Kerr-de Sitter and Kerr-anti-de Sitter black holes as accelerators for spinning particles. Phys. Rev. D **99**, 064022 (2019). https://doi.org/10.1103/PhysRevD.99.064022. arXiv:1812.10702 [gr-qc]

134. C.-H. Wang, C.-Q. Pang, S.-W. Wei, Extracting energy via magnetic reconnection from Kerr-de Sitter black holes. Phys. Rev. D **106**, 124050 (2022). https://doi.org/10.1103/PhysRevD.106.124050. arXiv:2209.08837 [gr-qc]

135. I. Dymnikova, A. Dobosz, B. Sołtysek, Classification of circular equatorial orbits around regular rotating black holes and solitons with the de Sitter/phantom interiors. Universe **8**, 65 (2022). https://doi.org/10.3390/universe8020065